Monthly Notices
of the
ROYAL ASTRONOMICAL SOCIETY
MNRAS **456,** 4191–4208 (2016) doi:10.1093/mnras/stv2859

A young star-forming galaxy at $z = 3.5$ with an extended Lyman α halo seen with MUSE

Vera Patrício,[1⋆] Johan Richard,[1⋆] Anne Verhamme,[1,2] Lutz Wisotzki,[3] Jarle Brinchmann,[4,5] Monica L. Turner,[4] Lise Christensen,[6] Peter M. Weilbacher,[3] Jérémy Blaizot,[1] Roland Bacon,[1] Thierry Contini,[7,8] David Lagattuta,[1] Sebastiano Cantalupo,[9] Benjamin Clément[1] and Geneviève Soucail[7,8]

[1]*CRAL, Observatoire de Lyon, Université Lyon 1, 9 Avenue Ch. André, F-69561 Saint Genis Laval Cedex, France*
[2]*Observatoire de Genève, Université de Genève, 51 Ch. des Maillettes, CH-1290 Versoix, Switzerland*
[3]*AIP, Leibniz-Institut für Astrophysik Potsdam (AIP) An der Sternwarte 16, D-14482 Potsdam, Germany*
[4]*Leiden Observatory, Leiden University, PO Box 9513, NL-2300 RA Leiden, Netherlands*
[5]*Instituto de Astrofísica e Ciências do Espaço, Universidade do Porto, CAUP, Rua das Estrelas, PT4150-762 Porto, Portugal*
[6]*Dark Cosmology Centre, Niels Bohr Institute, University of Copenhagen, Juliane Maries Vej 30, DK-2100 Copenhagen, Denmark*
[7]*IRAP, Institut de Recherche en Astrophysique et Planétologie, CNRS, 14, avenue Edouard Belin, F-31400 Toulouse, France*
[8]*Université de Toulouse, UPS-OMP, Toulouse, France*
[9]*ETH Zurich, Institute of Astronomy, HIT J 12.3, Wolfgang-Pauli-Str. 27, CH-8093 Zurich, Switzerland*

Accepted 2015 December 3. Received 2015 December 1; in original form 2015 October 2

ABSTRACT

Spatially resolved studies of high-redshift galaxies, an essential insight into galaxy formation processes, have been mostly limited to stacking or unusually bright objects. We present here the study of a typical (L^*, $M_\star = 6 \times 10^9$ M$_\odot$) young lensed galaxy at $z = 3.5$, observed with Multi Unit Spectroscopic Explorer (MUSE), for which we obtain 2D resolved spatial information of Lyα and, for the first time, of C III] emission. The exceptional signal-to-noise ratio of the data reveals UV emission and absorption lines rarely seen at these redshifts, allowing us to derive important physical properties ($T_e \sim 15600$ K, $n_e \sim 300$ cm^{-3}, covering fraction $f_c \sim 0.4$) using multiple diagnostics. Inferred stellar and gas-phase metallicities point towards a low-metallicity object ($Z_{\rm stellar} = \sim$0.07 Z$_\odot$ and $Z_{\rm ISM} < 0.16$ Z$_\odot$). The Lyα emission extends over $\sim$10 kpc across the galaxy and presents a very uniform spectral profile, showing only a small velocity shift which is unrelated to the intrinsic kinematics of the nebular emission. The Lyα extension is approximately four times larger than the continuum emission, and makes this object comparable to low-mass LAEs at low redshift, and more compact than the Lyman-break galaxies and Lyα emitters usually studied at high redshift. We model the Lyα line and surface brightness profile using a radiative transfer code in an expanding gas shell, finding that this model provides a good description of both observables.

Key words: techniques: imaging spectroscopy – galaxies: abundances – galaxies: high-redshift – galaxies: individual: SMACSJ2031.8-4036.

1 INTRODUCTION

During the past few decades, our understanding of galaxy formation and evolution has made significant progress thanks to the hundreds of high-redshift ($z > 3$) galaxies which have been detected in dedicated observing campaigns (e.g. Shapley et al. 2003; Vanzella et al. 2009; Stark et al. 2013). The main spectral feature used to confirm the distances of these galaxies is the Lyα emission, since it is the brightest emission line we can observe in distant sources. Unfortunately, many of these objects are too faint to show any other emission line at rest-frame UV wavelengths or, even less likely, continuum and absorption lines, offering a limited picture of the characteristics of high-redshift galaxies. The complexity of the Lyα resonant process, which depends not only on the gas dynamics but also on gas density and dust content, also requires the observation of non-resonant lines in order to robustly probe the physical properties of such galaxies.

Stacking techniques, which combine spectra or images of dozens or even hundreds of objects in order to increase signal-to-noise ratio (e.g. Shapley et al. 2003; Erb et al. 2014; Hayes et al. 2014;

⋆E-mail: vera.patricio@univ-lyon1.fr (VP); johan.richard@univ-lyon1.fr (JR)

Momose et al. 2014), allow the study of statistically significant properties of high-redshift galaxies. In particular, their rest-frame UV and optical nebular lines as well as their spatial extension both in continuum and in Lyα can be probed (Steidel et al. 2011), providing an essential clue to understand when most galaxies gather their mass. However, these techniques erase the structure, kinematics and other resolved properties of individual sources, and with it the possibility of learning something new about the detailed physical processes that shape galaxy evolution. Studies of the full 2D extent of Lyα emission in individual sources have been implemented with narrow-band imagers or integral-field unit spectrographs (IFU), but have generally focused on extreme objects such as giant Lyα blobs or powerful radio galaxies. The intrinsic brightness of these objects makes it possible to probe deeply into the physics of the gas, even to resolve the spatial variation of the Lyα line at kpc scales (e.g. Weijmans et al. 2010; Swinbank et al. 2015; Prescott et al. 2015), but ideally, one would like to pursue similar studies on typical high-redshift galaxies, which requires a very high signal-to-noise ratio only achievable with the next generation of ground-based optical and near-infrared telescopes.

One way forward is to focus on high-redshift lensed galaxies, since gravitational lensing not only boosts the total observed flux of the sources but also enlarges them, making them ideal targets for resolved properties studies. There is already a small but growing collection of such lensed galaxies studied in rest-frame UV from z = 1.4 to 4.9 (Pettini et al. 2002; Fosbury et al. 2003; Villar-Martín, Cerviño & González Delgado 2004; Cabanac, Valls-Gabaud & Lidman 2008; Quider et al. 2009; Dessauges-Zavadsky et al. 2010; Christensen et al. 2012a,b; Bayliss et al. 2014) that probe $L^\star$ type galaxies at a resolution impossible to achieve without the lensing effect. To date, many of these studies have been performed with long-slit spectroscopy, due to technological constraints, which allows properties such as metallicity, star formation rate and age to be derived but with limited spatially resolved information. IFU observations are therefore desirable in order to obtain a full 2D picture of such resolved properties in individual galaxies. However, even with magnification produced by lensing, this is also challenging from a technological point of view, and currently studies have focused mainly on $z < 3$ galaxies in the near-infrared (Stark et al. 2008; Yuan et al. 2011; Jones et al. 2013a). So far, there have only been two examples of such studies at $z > 3$: the $z = 5$ lensed galaxies in MS1358.4+6245 and RCS0224−0002 (Swinbank et al. 2007, 2009).

Combining gravitational lensing magnification with the unique efficiency of the MUSE (Multi Unit Spectroscopic Explorer) integral-field spectrograph it is already possible increase the number of resolved studies in high-redshift sources. Here we present the 2D morphology and kinematics of a $M_\star = 10^9\,\mathrm{M}_\odot$ galaxy as well as the analysis of emission and absorption features seldom accessible at these redshifts. This galaxy is a strongly lensed system of five images at $z = 3.5$ (Fig. 1), first reported by Christensen et al. (2012a). It was detected in the *Hubble Space Telescope* (*HST*)

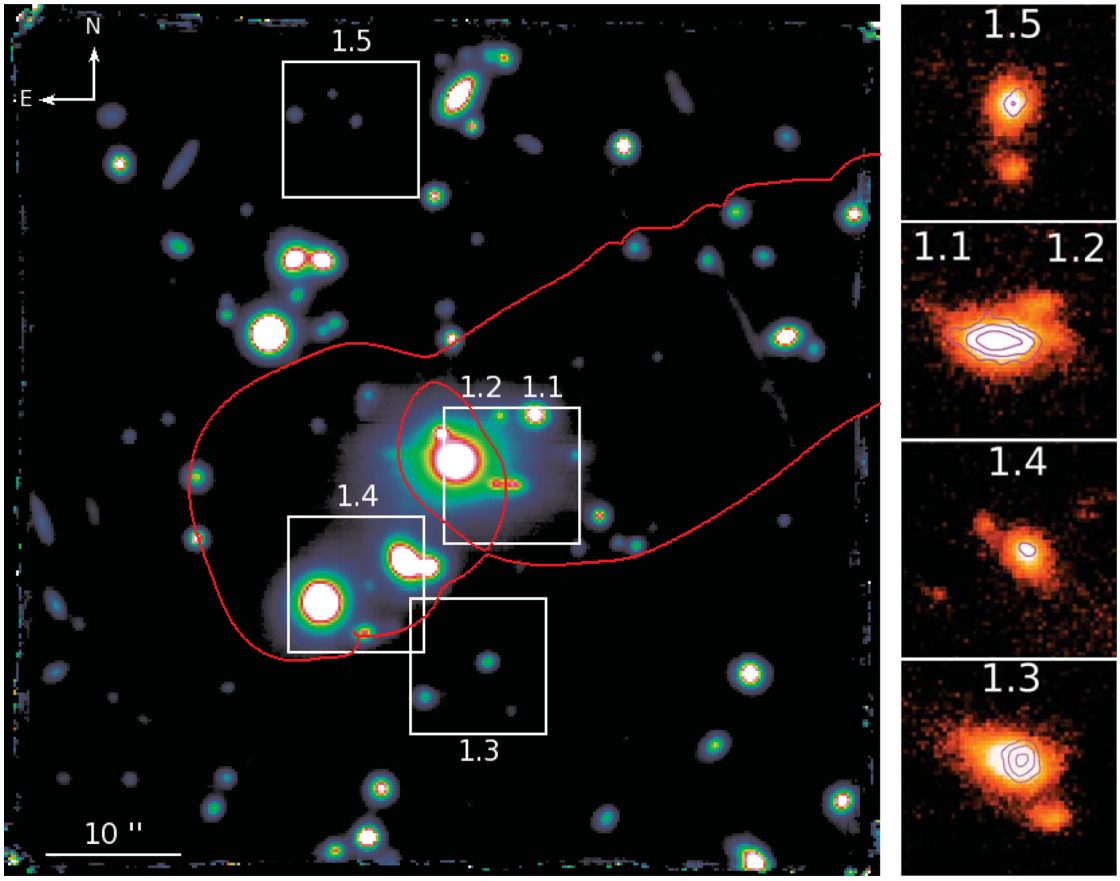

Figure 1. Left: MUSE white light (4750–9350 Å) image of the SMACS2031 cluster core. Red line: critical line of the mass model (from Richard et al. 2015), white squares: 10 × 10 arcsec^2 regions around multiple sources that were zoomed in to produce the right side images. Right: Lyα (5476–5494 Å) line images of system 1 multiple images with C III] (8578–8607 Å) contours overplotted in magenta. All five multiple images are seen in both Lyα and C III] line images. The Lyα emission extends up to 4 arcsec and a small companion, previously unknown, can be seen at about 3 arcsec of the main body in the Lyα line image.

image of the massive cluster SMACSJ2031.8-4036 obtained as part of SMACS, the Southern extension of the MAssive Cluster Survey (MACS; Ebeling, Edge & Henry 2001). New spectroscopic data were obtained during MUSE commissioning time, giving rise to an improved lens model of the cluster core (Richard et al. 2015).

The paper is organized as follows. In Section 2 we detail the observations and data reduction; in Section 3 we describe the data analysis, including the extraction of spectra and line images from the MUSE data cube. The results and discussion of spectral and morphological features are presented in Section 4, while detailed spectral modelling of the Lyα profiles and its interpretation are shown in Section 5. In Section 6 we summarize and conclude. Throughout this paper, we adopt a Λcold dark matter cosmology with Ω=0.7, $\Omega_{\rm m}$=0.3 and $H = 70$ km s^{-1} Mpc^{-1} and use proper transverse distances for sizes and impact parameters.

2 MUSE OBSERVATIONS AND DATA REDUCTION

MUSE is an integral-field optical spectrograph (4750 to 9350 Å in nominal mode) with a field of view of 1 $\times$1 arcmin^2 (Bacon et al. 2010). The field of view is divided into 24 sub-fields (*channels*) and each of them is sliced into 48 which are dispersed by a grating and projected on to the detector (one per channel). The data have a spatial sampling of 0.2 $\times$ 0.2 arcsec^2 and a spectral sampling of 1.25 Å for each voxel (volumetric pixel) in the final data cube. MUSE large field of view, and medium-resolution spectroscopy ($\sim$1500–3500), makes it particularly efficient in the study of gravitational lenses, since it simultaneously provides both the spatial location and redshift of multiply lensed images, which are essential for constraining the lensing models.

The data used in this paper were obtained over several nights of the second MUSE commissioning run, between 2014 April 30 and May 7. The observing strategy combined a small dithering pattern with rotations of the field of view. This was done in order to avoid systematics by minimizing the slice pattern that arises during the image reconstruction process from the small gaps between slices at the CCD level. The pointing coordinates were randomly selected from a box of 1.2 $\times$ 1.2 arcsec^2 centred on the cluster and the rotation angle was varied by 90° between two consecutive pointings. The instrumental wobble introduces an additional random offset of 0.1–0.3 arcsec. In total, 33 exposures of 1200 s each were acquired with a measured maximum offset of 0.82 arcsec in RA and 0.98 arcsec in Dec. from the central point.

The data reduction was performed with version 1.0 of the MUSE pipeline (Weilbacher et al. 2014). Basic calibration – which includes bias subtraction, flat fielding correction, wavelength and geometrical calibrations – is applied to individual exposures using the MUSE_BIAS, MUSE_FLAT, MUSE_WAVECAL and MUSE_SCIBASIC pipeline recipes. Calibration data were chosen to match, closely as possible, the instrument temperature of each exposure, since channel alignment is sensitive to this temperature. After these first processing steps, exposures are saved as 24 individual pixel tables, one per channel, listing the calibrated fluxes at each CCD pixel.

The next step is applying flux and astrometric corrections and combines the several channels of each exposure with the MUSE_SCIPOST recipe. The pipeline performs sky subtraction by fitting a model of the sky spectrum to the data and subtracting it. Several tests were performed with different fractions of the field-of-view used to estimate the sky spectrum and different spectral samplings of the continuum and lines, but since there were no significant quality differences between the several trials, we adopted the default parameters: 30 per cent of sky fraction, continuum and line sampling of 1.25 Å. This process results in 33 individual data cubes with 312 $\times$ 322 $\times$ 3681 voxels (spatial $\times$ spatial $\times$ spectral). Telluric correction, derived from the standard star, is also applied at this point of the reduction. Sky subtraction is furthermore improved using ZAP (Zurich Atmosphere Purge; Soto et al., in preparation), a principal component analysis method, aimed at removing systematics remaining after sky subtraction. ZAP estimates sky residuals in spatial regions free from bright continuum objects and subtracts these residuals in the entire field of view. Finally, several standard stars were reduced and their respective response curves produced and compared. We used them to calibrate the flux in science frames, rejecting response curves taken under non-photometric conditions.

Table 1. Exposure list with mean seeing of each night exposure measured around 6000 Å.

Date	Exposure time (s)	Seeing (arcsec)	Conditions
2014-04-30	6 $\times$ 1200	0.96	Photometric
2014-05-01	4 $\times$ 1200	1.09	Clear
2014-05-02	4 $\times$ 1200	1.23	Clear
2014-05-04	3 $\times$ 1200	0.85	Clear
2014-05-05	4 $\times$ 1200	0.86	Photometric
2014-05-06	7 $\times$ 1200	0.67	Photometric
2014-05-07	5 $\times$ 1200	0.58	Photometric
Combined cube	33 $\times$ 1200	0.72	

Before combining all 33 individual cubes into one single data cube, the sky transmittance during each exposure was estimated by measuring the integrated flux of the brightest stars in the field. The highest transmittance was taken as the photometric reference and in the final combination each exposure's flux was rescaled to match the reference. The positions of the stars were measured and used to correct the small offsets between exposures (due to the aforementioned instrumental wobbling) before averaging all cubes into a single data cube. A 3 σ-clipping rejection for cosmic rays was used during the combination and the combined cube was also corrected with ZAP. Since the background spectral shape was found not to be flat we estimated the median value of the background on each wavelength plane, by masking bright objects and averaging the 100 nearest planes (50 to the red and 50 to the blue), and then subtracted this value from the respective wavelength plane.

We measured the seeing by fitting a 2D circular moffat profile to the brightest star, obtaining full width at half maximum (FWHM) values in the combined cube of 0.72 and 0.63 arcsec at 6000 and 9000 Å, respectively (see Table 1 for details of individual exposures), with a wavelength dependence similar to the deep MUSE data from Bacon et al. (2015). Photometry was checked to be in accordance with the *HST* data up to 8 per cent by comparing the flux of the brightest star measured on *HST* data and on an equivalent image produced by integrating the MUSE cube using the *HST* transmittance filter. The variance is propagated by the pipeline trough the reduction process for each individual CCD pixel, resulting in a final cube with a variance value associated with each voxel.

3 DATA ANALYSIS

In this section we describe the steps taken to extract emission line images and spectra needed to measure the spectrophotometric properties of the system from the MUSE data cube. Since this is a lensed

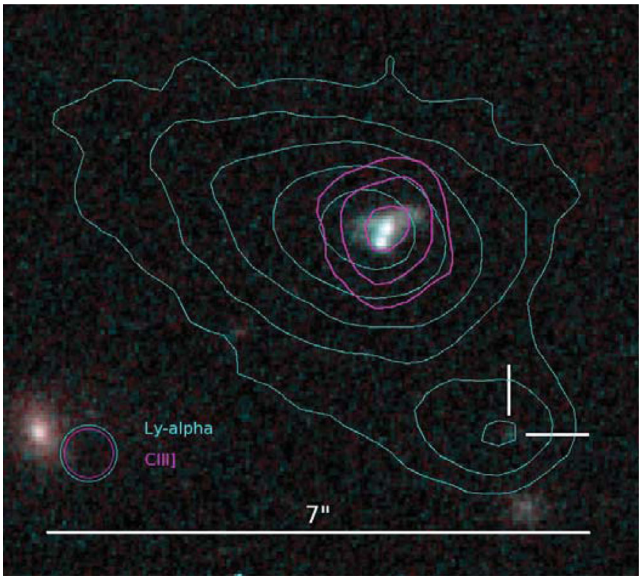

Figure 2. Image 1.3 in the *HST* $V+I$ band, with Lyα (cyan) and C III] (magenta) MUSE contours in geometric scale from 3 to 50 σ. The white cross marks the location of the faint companion in *HST* (F814W ∼28 AB), clearly detected with MUSE. Although C III] peaks at the same location has the *HST* continuum, Lyα appears offset by ∼0.4 arcsec. The bottom left circles show the FWHM of the MUSE PSF.

system, we also detail the corrections applied to recover the undistorted morphology of the galaxy as well as its intrinsic flux.

3.1 Line image analysis

In order to study the Lyα emission morphology we extract an image around the Lyα line (5480–5490 Å, observed) from the data cube, choosing the spectral width that maximize its signal-to-noise ratio. We correct this image by subtracting a continuum line image, produced by averaging two other images, one blueward and the other redward of Lyα. An equivalent procedure is used to create a line image of the C III] emission (8580–8595 Å), carefully choosing the red and blue continuum images to avoid emission lines and sky residuals.

All five multiple images of system 1 detected with *HST* are seen both in Lyα and C III] line images, with smaller spatial extension in C III] and an offset of up to ∼0.4 arcsec between the Lyα and C III] peaks (see Fig. 2). We adopt the same nomenclature as Richard et al. (2015) to refer to the multiple images, from the most magnified image – 1.1 and 1.2 – to the least. All multiple images show consistent spatially extended emission in Lyα up to 4 arcsec in image 1.3. A small companion (identified as system 2 in Richard et al. 2015) is also clearly visible near each image, about 2.3–3.2 arcsec away from the main component, and is associated with a very faint (F814W ∼ 28 AB) *HST* point source (Fig. 2).

3.2 Source plane reconstruction

We use the well-constrained mass model derived from the 12 multiple image systems identified in the *HST* image and detected in the MUSE data cube (Richard et al. 2015) to demagnify the images and recover the intrinsic source morphology. This is done by inverting the lens equation and putting the observed pixels on a regular source plane grid, while conserving surface brightness. All five multiple images are comparable to each other in the source plane, though some small differences in configuration arise due to the position of the caustic lines along the extension of the galaxy and the source plane point spread function (PSF) shape (see Fig. 3). The small offset between Lyα and continuum peak emission is confirmed in all images (∼0.6 kpc). The relative position of the companion in all five multiple images is well reproduced by the model, which confirms that this smaller source is physically close to the main body (∼11.2 kpc). The companion is approximately seven times intrinsically fainter in Lyα than the main body and it is not detected in the C III] line image. This is confirmed in the 1D spectrum, where no other emission line besides Lyα is detected (see Section 4.1).

Although images 1.1 and 1.2 have a very high magnification factor, since they are very close to the critical line, neither is a complete image of the original source. Conversely, image 1.3, the second brightest image, is very nearly a complete image of the source, thus we will focus the spatial analysis on this observation. Image 1.5 is the only truly complete image of the galaxy, but is also the least magnified. In this multiple image, an additional, faint, Lyα structure can be seen towards the north-east (green circle in the right panel of Fig. 3), which is not expected to be seen in images 1.1, 1.2 and 1.3 since it lies outside of the caustic line.

3.3 Spectrum extraction and magnification factors

To maximize the signal-to-noise ratio in the extracted spectrum, we use the C III] line image to define a 3σ surface brightness threshold at $\sim 2.8 \times 10^{-19}$ erg s^{-1} cm^{-2} arcsec^{-2}. This level encloses three compact regions at the peak of images 1.1, 1.2 and 1.3, all probing the same physical region in the source plane (within 500 pc) despite having different magnification factors. Light contamination by cluster members is a concern at the location of images 1.1 and 1.2 and we correct it by subtracting a scaled cluster member spectrum, using the spectral slope of image 1.3 (further from cluster members) as a reference. We find that the continuum slope of this decontaminated spectrum is in good agreement with the fit from Christensen et al.

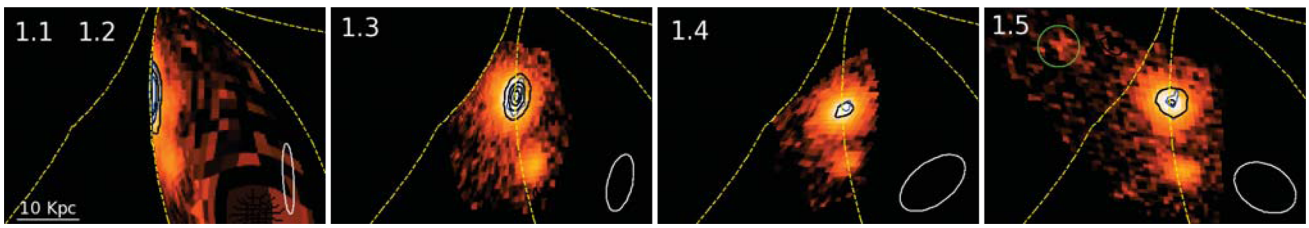

Figure 3. Source plane reconstruction of the Lyαline image. Dashed yellow: caustic lines. Blue contours: C III] line image reconstruction. Black contours: continuum near Lyαimage reconstruction. The ellipses on the lower right corners correspond to the source plane PSF, obtained by reconstructing the 2D moffat profile of the measured seeing (at the wavelength of Lyα) into the source plane. The small differences between the source plane images are well explained by the different PSF shapes. Note that images 1.1 and 1.2 are radial images and only cover the western half of the source.

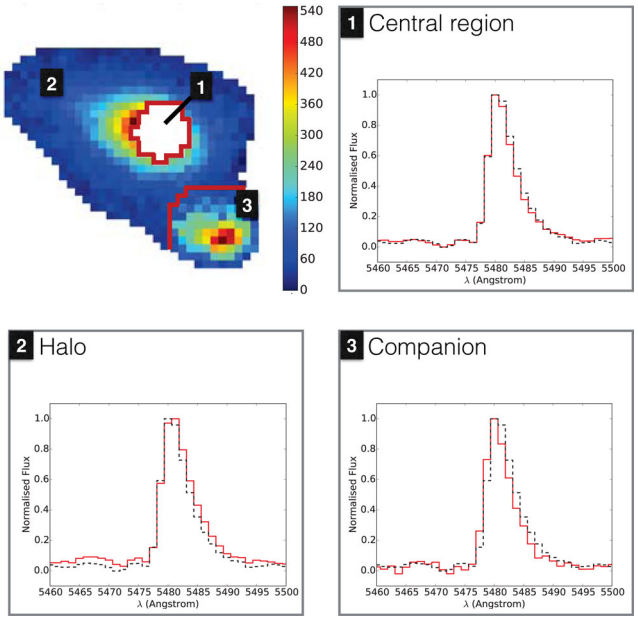

Figure 4. The three extraction regions shown for image 1.3: central (1) in white, halo (2) in colour and companion (3) also in colour (colour bar encodes the observed Lyα surface brightness). The extraction region of the total spectrum corresponds to the sum of regions 1 and 2. The panels show the Lyα line of regions 1 to 3 and the one extracted from the total region (in dashed black).

(2012a), who obtained a slit spectrum of the central part of image 1.2.

After extracting this high signal-to-noise ratio spectrum (which throughout the analysis is referred to as the *combined spectrum*), we investigate differences between spectra extracted from different locations, focusing on image 1.3. Inspecting the spectral profile of Lyα on a pixel-by-pixel basis, we find that – remarkably – all profiles have a similar appearance, regardless of their location in the galaxy. This motivated us to extract spectra from regions where physical differences would be expected. In particular, we choose to explore two different regions: the central part of the galaxy, with strong C III] and continuum emission, and the outer part (halo), containing Lyα emission.

We start with the previously defined C III] regions and extract a *central* spectrum in image 1.3. We then define in a similar way a more extended region containing the full extent of detected Lyα emission, excluding the companion. A 2σ threshold in the Lyα line image ($\sim 3.75 \times 10^{-19}$ erg s^{-1} cm^{-2} arcsec^{-2}) defines this *total* spectrum (see upper left panel of Fig. 4). The *halo* spectrum is defined by excluding the central region from this total spectrum. Due to the seeing, we estimate 38 per cent of the central continuum emission to be present in the halo spectrum, which we correct by rescaling the central spectrum flux to include this missing fraction, and correct the halo spectrum to remove the contribution from the central region. Finally, the spectrum of the companion is selected by defining a circular region of 1.2 arcsec radius centred on the brightest pixel of image 1.3, and the respective spectra are extracted.

In total, the extraction results in the five following spectra that we use in the following sections to derive the physical properties of the system:

(i) *Combined:* with maximum signal-to-noise ratio, achieved by combining the central region of images 1.1, 1.2 and 1.3;

(ii) *Total*: extracted from an extended region of image 1.3 based on the Lyα line image;

(iii) *Central:* extracted from the central region of image 1.3 based on the C III] line image;

(iv) *Halo:* extracted from the total region of image 1.3 but excluding the central region;

(v) *Companion:* nearby compact source detected in Lyα line image (see Fig. 2).

The magnification factors of the several regions needed to recover the intrinsic fluxes of these spectra were calculated using the Richard et al. (2015) mass model. Images 1.1 and 1.2 are a special case, since they do not image the entire galaxy: the central region corresponds only to 43 per cent of the total image and the extended region (defined in Lyα) to 37 per cent. Taking these factors into account, we estimate a total magnification factor of 26 for the combined spectra. After magnification correction, the central region contains 40 $\pm$ 2 per cent of the total flux and the halo 60 $\pm$ 2 per cent.

In the following sections the detailed physical properties of this object will be discussed in detail. With a magnification-corrected rest-frame UV magnitude of -21.14 AB, this galaxy has a typical L* luminosity at this redshift (Steidel et al. 2011). It has a global equivalent width of 32 Å, classifying it as a Lyα emitter, and a Lyα luminosity of 5.6×10^{42} erg s^{-1}, similar to the typical luminosity of narrow band surveys for redshifts $z \sim 3$ (Garel, Guiderdoni & Blaizot 2015).

4 RESULTS AND DISCUSSION

In this section, we present and discuss the integrated properties that can be derived from the spectral analysis of the combined spectrum, such as temperature, density and metallicity. We then focus on the resolved properties of image 1.3, comparing Lyα with continuum and C III] emission.

4.1 Spectral features

To derive the integrated properties we make use of the combined spectrum, which corresponds to the central region of the galaxy, but has higher signal-to-noise ratio than the central spectrum of image 1.3 alone (see Fig. 5). We measure a systemic redshift of 3.506 18 $\pm$ 0.000 05 by simultaneously fitting the strongest available emission lines – He II λ1640 , O III] $\lambda\lambda$1661, 66 and C III] $\lambda\lambda$1907, 09. Christensen et al. (2012a) report $z = 3.5073$ from multiple emission lines but the small difference is due to an incorrect heliocentric–barycentric velocity correction in their analysis. Line properties are measured by fitting a Gaussian profile to emission lines and a constrained Gaussian fit to the C III] doublet, fixing the wavelength ratio between lines to its theoretical value. As for the Lyα emission line, and some absorption lines where the profile was clearly asymmetric, we defined an *asymmetric Gaussian profile* by allowing the FWHM of two half Gaussians to freely vary, while forcing the peak value of both to coincide at the same wavelength. Instead of using the pipeline-propagated variance to estimate the errors, as it does not include noise correlation, we generate 500 realizations of the observed spectrum, by randomly picking the flux level at each wavelength from a Gaussian distribution. The mean of this Gaussian distribution is the observed spectrum intensity and its sigma is the pipeline-propagated error. The absolute value of the error was scaled so that the realizations would keep the same signal-to-noise ratio as the observed continuum spectrum, so that

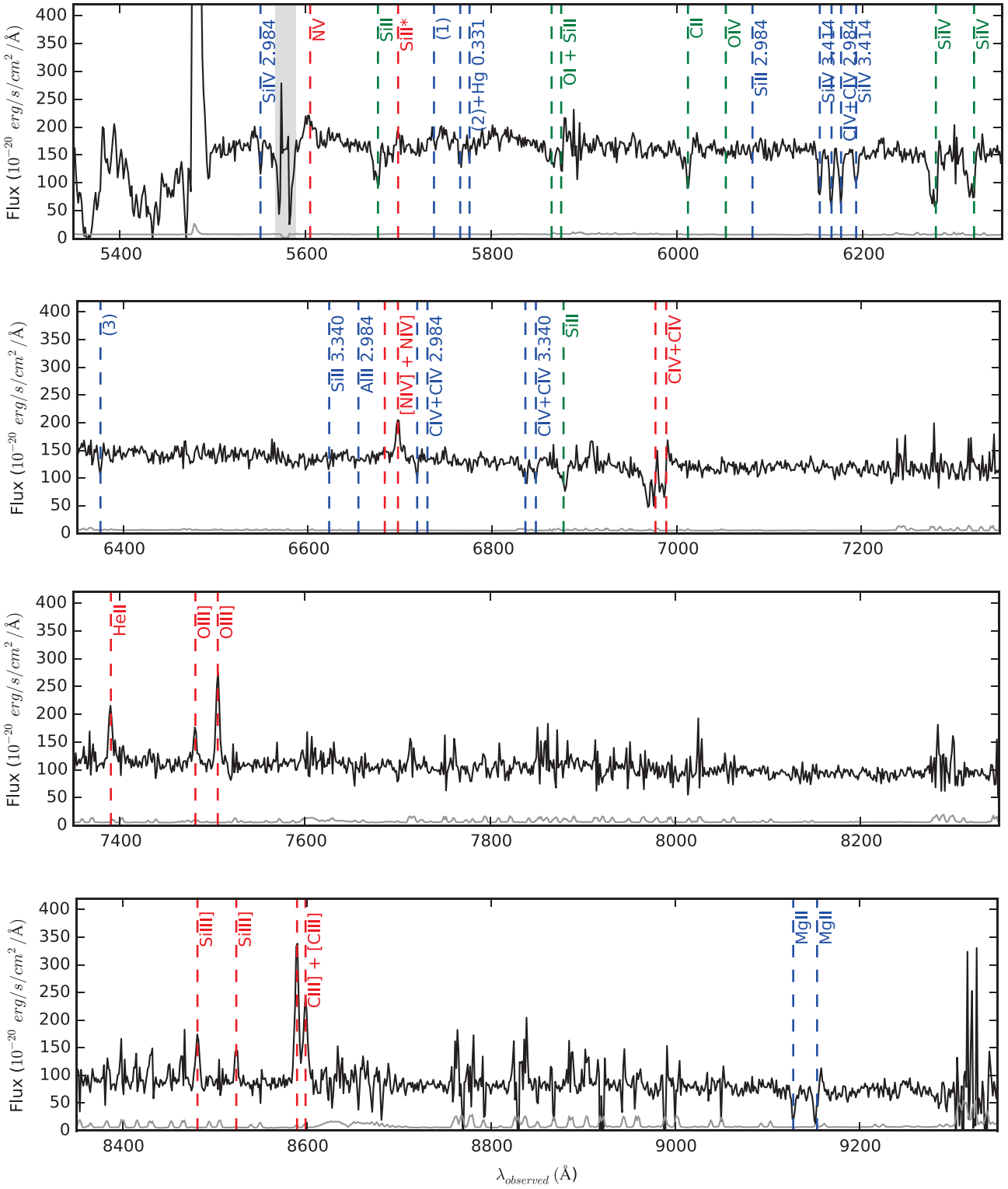

Figure 5. Spectral lines identified in the central region spectrum. Black: observed spectrum central region. Grey line: pipeline-propagated variance. Shaded grey: strong sky residuals. Green dashed lines: absorption lines associated with the $z = 3.5$ galaxy. Red dashed lines: emission lines associated with the same system. Blue dashed lines: other absorption lines, some of which we associate with intervening systems over the line of sight (see Appendix A). Besides the Lyα C III] and O III] emission lines, several other emission lines, more rarely seen at higher redshifts, were identified, such as the Si III], Si II* and the N IV] doublet. The magnification provided by lensing as well as the combination of spectra from several multiple images, provides a high signal-to-noise ratio also in the continuum, allowing the confident identification of several Si, C and O absorption lines.

Table 2. Lyα line measurements on image 1.3 (total, centre and halo; see Fig. 4) and on the combined (high signal-to-noise ratio) spectrum from all multiple images. Observed fluxes are *uncorrected* for magnification and EW are given in rest frame. Δv is relative to the systemic redshift. μ is the magnification factor of the corresponding region. *Estimated from the F814W photometry.

	Flux 10^{-18} (erg s^{-1} cm^{-2})	EW (Å)	FWHM (km s^{-1})	Δv (km s^{-1})	μ
Total	409 ± 11	32 ± 4	248	176 ± 9	8.5
Centre	205 ± 8	20 ± 2	225	172 ± 9	7.4
Halo	206 ± 4	49 ± 12	260	178 ± 9	8.6
Companion	41 ± 6	360 ± 70*	247	156 ± 10	5.1
Combined	526 ± 6	18 ± 24	216	186 ± 9	26

Table 3. Emission line measurements from the central region spectrum combining signal from all multiple images. Flux corresponds to observed flux (without magnification correction). Observed wavelengths (λ_{obs}) are given in air and σ was corrected for instrumental broadening.

Line	λ_{rest} (Å)	λ_{obs} (Å)	Flux $\times 10^{-20}$ (erg s^{-1} cm^{-2})	σ (km s^{-1})	EW (Å)
Lyα	1215.67	5479.02 ± 0.25	51100 ± 165	110.5 ± 0.8	17.22 ± 2.44
N V	1242.80	5604.83 ± 0.41	2560 ± 138	257.9 ± 14.0	0.67 ± 0.04
Si II*	1264.74	5699.55 ± 0.97	417 ± 103	24.8 ± 20.2	0.11 ± 0.01
[N IV]	1483.32	6683.47 ± 0.25	613 ± 58	104.0 ± 4.2	0.21 ± 0.02
N IV]	1486.50	6697.77 ± 0.25	2996 ± 80	103.7 ± 4.2	1.04 ± 0.05
He II	1640.42	7390.39 ± 0.28	2301 ± 114	76.9 ± 6.7	0.99 ± 0.10
O III]	1660.81	7481.77 ± 0.27	1479 ± 92	58.6 ± 6.2	0.65 ± 0.05
O III]	1666.15	7505.92 ± 0.25	3002 ± 56	54.1 ± 1.4	1.33 ± 0.09
[Si III]	1881.96	8481.49 ± 0.26	1363 ± 52	55.3 ± 2.7	0.81 ± 0.06
Si III]	1892.03	8523.66 ± 0.28	1105 ± 66	62.2 ± 4.2	0.67 ± 0.05
[C III]	1906.68	8589.61 ± 0.25	5090 ± 72	60.0 ± 1.0	3.14 ± 0.19
C III]	1908.73	8598.84 ± 0.25	3417 ± 77	59.9 ± 1.0	2.11 ± 0.13

Table 4. Absorption line measurements from the central region spectrum combining signal from all multiple images. Flux corresponds to observed flux (without magnification correction). Observed wavelengths (λ_{obs}) are given in air and σ is corrected for instrumental broadening.

Line	λ_{rest} (Å)	λ_{obs} (Å)	σ (km s^{-1})	EW (Å)
Si II	1260.42	5677.84 ± 0.49	166.1 ± 23.9	0.70 ± 0.036
O I	1302.17	5864.89 ± 0.27	218.6 ± 12.6	0.31 ± 0.031
Si II	1304.37	5875.20 ± 0.43	14.9 ± 15.2	0.09 ± 0.003
C II	1334.53	6011.75 ± 0.35	119.0 ± 14.9	0.61 ± 0.033
O IV	1342.99	6052.54 ± 1.80	148.0 ± 60.7	0.22 ± 0.021
Si IV	1393.76	6278.77 ± 0.28	153.2 ± 7.5	1.21 ± 0.052
Si IV	1402.77	6319.90 ± 0.51	130.7 ± 13.7	0.94 ± 0.099
Si II	1526.71	6877.29 ± 0.30	120.1 ± 4.9	0.47 ± 0.215

we empirically reproduce pixel correlation. The wavelength calibration error (0.03 Å) was added in quadrature to error estimations of the line peaks. Results for the combined spectrum are listed in Tables 2, 3 and 4.

The most noticeable characteristic of the four Lyα profiles from the different regions defined in image 1.3 – central, halo, total and companion (see Fig. 4) – is how similar they all look: the line profile is clearly asymmetric with very close velocity shifts relative to the systemic redshift ($\sim$178 km s^{-1}), except the companion, which is slightly blueshifted ($\sim$20 km s^{-1}) relative to the other three spectra (see Table 2). A similar result has been reported by Swinbank et al. (2007) in a $z = 4.88$ lensed galaxy and in the local galaxy Haro 2 (Mas-Hesse et al. 2003).

Unlike the companion and halo spectra, which do not show any other prominent line besides Lyα the central spectrum displays a wealth of other emission lines, which can be used to derive many integrated properties. We identify the following lines: the O III] $\lambda\lambda$1661, 66and C III] $\lambda\lambda$1907, 09 doublets which are clearly resolved, the N IV] $\lambda\lambda$1483, 86 doublet and the He II λ1640 line, previously undetected in Christensen et al. (2012a; see Fig. 5) and Si II λ1882, 92. Also worth noticing is the Si II* emission line, a fine structure transition line also reported by Erb et al. (2010) in a low-metallicity $z = 2.3$ lensed galaxy and in local galaxies (e.g. Lyman Alpha Reference Sample, LARS; Rivera-Thorsen et al. 2015) and Green Peas galaxies (Henry et al. 2015).

The average intrinsic velocity dispersion, after correcting for the line spread function (LSF), is 61 ± 8 km s^{-1}, excluding the N V] line and the N IV] doublet that show a higher dispersion. Our data also confirm that there is no AGN present in this system, since the measure a C III]/Lyα ratio of 0.07, much lower than the 0.125 value measured in a sample of narrow-line AGN LBG (Shapley et al. 2003). Finally, we derive a rest-frame UV absolute magnitude of -21.1 AB (magnification corrected and assuming no extinction), equivalent to an L* galaxy at this redshift. Using the Kennicutt (1998) conversion (SFR $= L_{\nu} \times 1.4\,10^{-28}$), assuming a Salpeter IMF, we obtain a current, magnification-corrected, SFR of $\sim$17.5 $M_{\odot}$ yr^{-1}.

The extraordinary quality of the data also reveals absorption lines at high signal-to-noise ratio, many of them sufficiently resolved to clearly display an asymmetric profile, with an elongated blue tail, generally interpreted as tracing absorption by outflowing material (e.g. Shapley et al. 2003). In our case, the maximum of absorption seems to arise from static gas: we did not find any velocity shift of the peak of the low ionization absorption lines (Si II

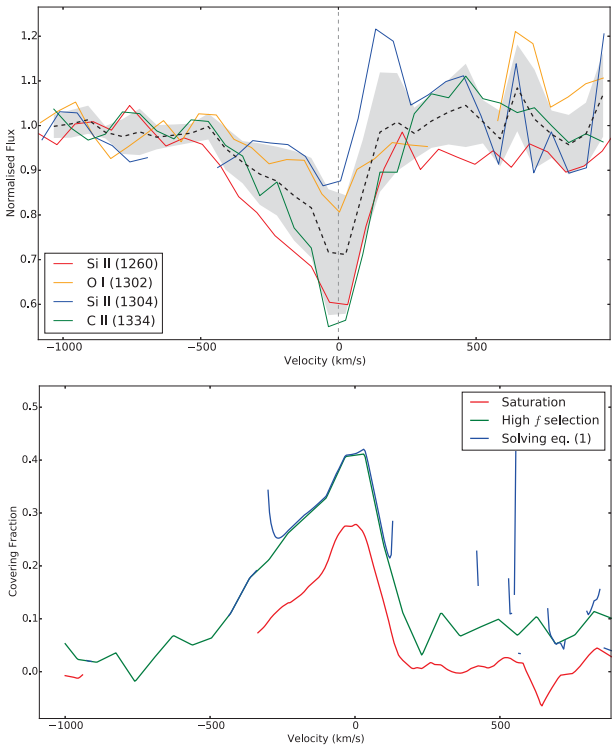

Figure 6. Upper panel: low ionization absorption lines on rest velocity frame. Black: mean profile with standard deviation in grey shadow. The maximum absorption at zero velocity suggests that most of the neutral gas is at rest, although the extended blue wind indicates that some outflowing gas is also present. Lower panel: covering fraction derived by three different methods. Blue: directly fitting equation 1 to the Si II λ1260, Si II λ1304, Si II λ1526lines. Red: using all low ionization lines from the first panel and calculating covering fraction assuming saturation. Green: selecting only the lines with the highest oscillator strengths (Si II λ1260($f \sim 1.22$), C II λ1334 ($f \sim 0.13$) and Si II λ1526($f \sim 0.13$), and assuming saturation. Comparing the solution found by directly solving equation (1) with all available lines under the saturation assumption, it is clear that not all elements are saturated. By selecting the elements with the highest oscillator strength (hence more easily saturated) a much better agreement is achieved.

λ1260, Si II λ1302, Si II λ1304, C II λ1334 and Si II λ1526) with respect to the systemic redshift (see Fig. 6). We follow an equivalent procedure to fit the absorption lines as the one described above for the emission lines, except that we used an asymmetric profile, constructed as two half Gaussians with independent FWHM but the same peak intensity, to fit the strongest absorption lines. From these measurements we derive a larger velocity dispersion for the absorptions (150 ± 18 km s^{-1}) compared to the emission lines.

A number of strong absorption lines appear in the spectrum at wavelengths which do not match with any feature of the 3.5062 redshift system. They are most likely due to absorptions produced by systems within the line of sight. Indeed, we confidently identified three pairs of absorption lines as Si IV λ1394, 1403and C IV λ1548, 51doublets, due to their characteristic line ratios, and the derived redshifts are a good match to the redshift of single image s2 ($z = 2.982$), multiple-image systems 4 ($z = 3.340$) and 12 ($z = 3.414$) from Richard et al. (2015). We present a brief analysis of these intervening absorbers in Appendix A.

4.2 Physical parameters from integrated spectrum

The following subsections are dedicated to the analysis of the properties of the emission and absorption lines, from which we derive the gas density, temperature and covering fraction, as well as the analysis of the continuum, from which we derive the stellar population content of the galaxy and estimate metallicity. Within this section we use the combined spectrum, described in Section 3.

4.2.1 Temperature and density from line ratio diagnostics

From the MUSE data, we have access to four line ratio diagnostics, which we complement with previous X-Shooter results (Christensen et al. 2012b) to obtain a more comprehensive view. Three electron density diagnostics come from MUSE data exclusively – N IV] λ1483/λ1486 , Si III] λ1883/λ1892 and C III] λ1907/λ1909 – for which we measure ratios of 0.204 ± 0.025, 1.228 ± 0.120 and 1.490 ± 0.055, respectively. We update the previous electron temperature measurement from the O III] λλ1661, 66/O III] λ5009diagnostic by combining both data sets. To do this, we rescale the X-Shooter line fluxes so that the strong C III] doublet has the same intensity as the MUSE spectrum, and we measure an O III] λλ1661, 66/O III] λ5009ratio of 0.061 ± 0.003 (reddening corrected $E(B-V)$=0.03 obtained by Christensen et al. (2012b). Using the PYNEB package (Luridiana, Morisset & Shaw 2012) we study the possible temperature and density combinations for these line ratios also including the O II] λ3729/λ3726 diagnostic reported in Christensen et al. (2012b) (see Fig. 7). We find that the O II] λ3729/λ3726 , O III] λλ1661, 66/ O III] λ5009and C III] λ1907/λ1909 diagnostics are compatible and indicate a gas temperature of 16500 ±200 K and a density of ∼300 ± 700 cm^{-3} where the errors were estimated from the region limits where the several diagnostics (except for N IV]) agree. This temperature is well within the typical values found for other high-redshift lensed galaxies – 13 000 to 25 000 K (Villar-Martín et al. 2004; Erb et al. 2010; James et al. 2014). On the other hand, the density is lower than what was measured in other lensed galaxies, that nevertheless span a large range of values: from 600 to 5000 cm^{-3} for the Clone, the Cosmic Horseshoe and J0900+2234 lensed galaxies (Hainline et al. 2009; Bian et al. 2010; Wuyts et al. 2012). The

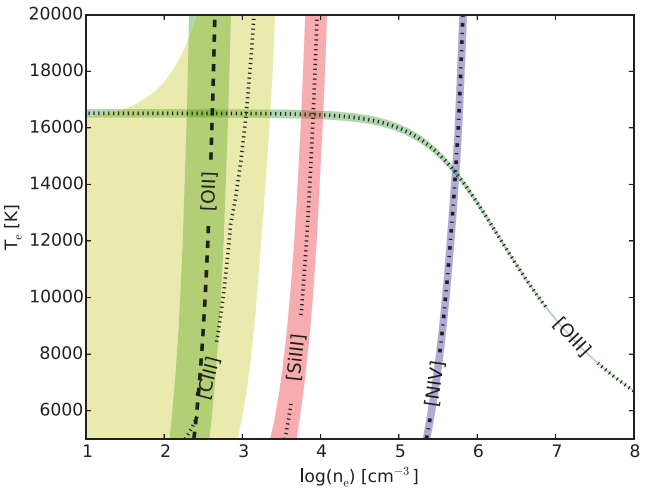

Figure 7. Range of electron density and temperature allowed by our emission line ratio diagnostics. Most diagnostics agree on a temperature of ∼16 500 K and an electron density of ∼300 cm^{-3}. The discrepancy of the N IV] λλ1483, 86 diagnostic can be due to its higher ionization energy, which would limit it to probe higher density regions (closer to the ionizing source).

$\sim$300 cm^{-3} we obtain are more typical of giant H II regions in the nearby Universe and are also consistent with the typical density (100 cm^{-3}) found in low-metallicity local galaxies with compact H II regions (Morales-Luis et al. 2014).

Contrastingly, the N IV] $\lambda\lambda$1483, 86 electron density diagnostic points to a much higher density ($>10^5$ cm^{-3}) at this temperature. Discrepancies between line diagnostics have been previously reported in high-redshift studies (e.g. Villar-Martín et al. 2004) with one possible explanation for this being the local variations in density and temperature within the galaxy, which are not disentangled in an integrated spectrum, resulting in incompatible diagnostic results. To test if any spatial variation of local density and temperature could be seen within the MUSE data, we measure the C III] λ1907/λ1909 ratio at several spatial positions in the central part of the galaxy, but found no significant change, with a ratio varying between 1.533 and 1.536. Another possible explanation is that N^{3+} is a higher ionization line, thus probing higher ionization zones, that can have a considerably higher density, which could explain why this diagnostic points to a higher density compared to the ones from lower ionization lines.

4.2.2 Neutral gas covering fraction

In this subsection we derive the neutral gas covering fraction from absorption lines depth. For a particular velocity bin, the intensity of the absorption lines can be related to the covering fraction by the following equation:

$$I = 1 - f_c \left(1 - \exp\left(\frac{-f\,\lambda\,N}{3.768 \times 10^{14}}\right)\right) \quad (1)$$

where I is the observed line intensity normalized to the continuum level, f_c the covering fraction, f the oscillator strength, λ the transition wavelength and N the column density. Jones et al. (2013b) discuss two possible approaches to derive the covering fraction with this equation: using at least two low-ionization lines and solving the system for the density and covering fraction or assuming that the lines are saturated ($\lambda N \gg 3.768 \times 10^{14}$) which simplifies expression (1) to $I = 1 - f_c$. We follow both procedures, using Si II λ1260, Si II λ1304and Si II λ1526lines to derive a covering fraction solving equation (1) (see Fig. 6). For the saturation assumption, we made a first test averaging all low-ionization lines: the three aforementioned Si II lines as well as Si II λ1302and C II λ1334 and directly calculating the covering fraction. From this average we obtain a lower covering fraction for every velocity bin, which indicates that the saturation assumption is not valid, at least, for all lines. We repeat the same method, this time only using the lines with higher oscillator strengths (hence more easily saturated): Si II λ1260, Si II λ1304and Si II λ1526lines. The covering fraction obtained with the average profile of these lines (lower panel of Fig. 6) is in good agreement with the result obtained without the approximation, suggesting that these three Si II lines must be close to saturation.

We obtain a maximum covering fraction of 0.4 at v= 0 km s^{-1} which suggests most of the neutral gas in this galaxy is at rest. However, it should be noticed that a covering fraction smaller than 1 in each velocity bin does not allow us to conclude that the global covering fraction of the gas traced is lower than 1 (see fig. 17 in Rivera-Thorsen et al. 2015, for an illustration). Given the shape of the Lyα profile emergent from this galaxy, the covering fraction of the scattering medium is most certainly 1, since the profile does not peak at the systemic redshift, but is redshifted by $\sim$170 km s^{-1}, which means no intrinsic Lyα emission is seen (Behrens, Dijkstra & Niemeyer 2014; Verhamme et al. 2015).

We also compare this system with the sample of $z \sim 4$ lensed galaxies analysed by Jones et al. (2013b), where the evolution of the maximum outflow velocity and maximum absorption depth with redshift is analysed (fig. 5 of the cited paper). The values that we obtain for this particular galaxy, -500 km s^{-1} for the maximum velocity where outflowing gas is still present and maximum covering fraction of 0.4, are in good agreement with the $z \sim 4$ sample presented. In the same work, a correlation of the maximum absorption depth with Lyα equivalent width is presented and, once more, our results agree with the derived correlation.

4.2.3 Stellar populations

The continuum signal from this magnified galaxy is also high enough to allow us to probe stellar populations. We chose to do so with the full spectral fitting technique, using the STARLIGHT code (Cid Fernandes et al. 2005) that produces a model spectrum from a linear combination of simple stellar population spectra, convolved with a kinematic kernel and corrected for extinction, to find the stellar population model that best matches an observed spectrum. STARBURST99 (Leitherer et al. 1999) stellar populations were used as templates to fit the spectrum, with absolute metallicities of 0.001, 0.002, 0.008, 0.014 and 0.040 and ages between 2 Myr and 3 Gyr. We prefer instantaneous burst models, since continuous star formation models are not simple to interpret in this linear combination method, and use the Geneva tracks with zero rotation and the Kroupa (2001) IMF. The Calzetti (Calzetti et al. 2000) extinction law is adopted in all fits.

We build six different libraries of stellar populations, which are used to independently fit the observations: five with a single metallicity spanning ages from 2 Myr to 3 Gyr, and one with an equal number of models of each metallicity, but with ages only from 2 to 600 Myr and a coarser time grid than the single metallicities libraries. To estimate errors, we generate 100 realizations of the observed spectra (using the same method as described in Section 4.1) and perform the fit with the same parameters, taking the errors as the standard deviation of the 100 results. All emission lines are masked before the fit, as well as all absorption lines confidently identified as features of systems in the line of sight. We also masked stellar winds and ISM lines (not easily reproduced by UV spectral models) but this did not affect the results of the fit.

All five model spectra from the single-metallicity libraries provide similar fits to the data (upper panel of Fig. 8), which confirms that precise metallicity estimations are hard to obtain from full spectral fitting in the UV. The models fail to correctly reproduce the intensity of the observed N V emission, where models predict a fainter emission, although as broad as seen in the observed spectrum. They also do not reproduce the complex C IV] profile, which is not surprising given that this line is a mixture of stellar and ISM emission and highly dependent on stellar winds, which are still poorly modelled. On the other hand, other absorption features such as Si II λ1260, C II λ1334 are well reproduced by all models. The different libraries also give comparable results: most of the flux can be reproduced by very young populations with ages up to 10 Myr (middle panel of Fig. 8), whereas most of the mass is created at $>$100 Myr lookback time (lower panel of the same figure). The model with all available metallicities has a very similar spectral shape to the others, and also shows a strong burst at 10 Myr and most mass ($\sim$98 per cent) being created between 300 and 350 Myr, with exclusively the lowest metallicity populations (Z=0.001). This preference for lower metallicity stellar populations in the mixed library and the fact that

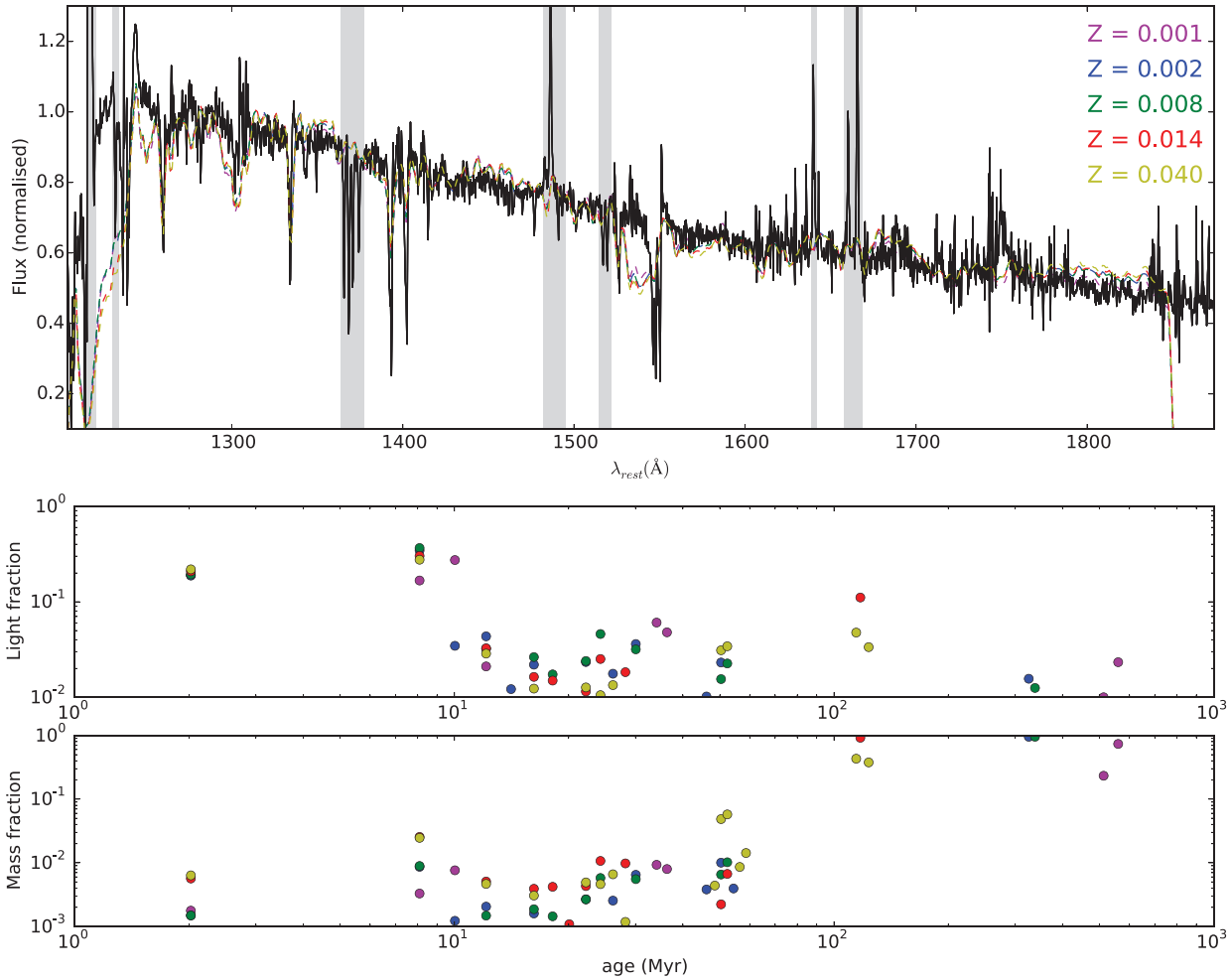

Figure 8. Upper panel: five stellar population models obtained with the individual metallicity libraries. Model spectra in colour, observed spectrum in black and masked regions in shaded grey. Despite small differences, all models equally reproduce the continuum and fail to reproduce wind emission features such as C IV λ1548, 51. Lower panels: single stellar populations – age in abscissa and metallicity colour coded – used in each of the five stellar spectrum, with the same colour as the above panel. The middle panel presents the contribution to the model of each individual stellar population in flux and the lower panel the contribution in mass. Despite the different age distributions of each model they all display a strong star-forming period at around 10 Myr and predict that most of the stellar mass (>80 per cent) was created 100 and 600 Myr of lookback time.

Table 5. Stellar population fits results. From left to right: absolute and solar metallicities, reduced χ^2, initial stellar mass and current stellar mass (accounting for mass losses due to SNe and winds), extinction. Errors are the standard deviation of fits performed on 100 realizations of the observed spectrum (see Section 4.1)

Z	$Z/Z_\odot$	χ^2	$10^9\,M_{\rm ini}/M_\odot$	$10^9\,M_{\rm cur}/M_\odot$	$E(B-V)$(mag)
0.001	0.07	2.11	8.2 ± 0.2	6.7 ± 0.2	0.016 ± 0.001
0.002	0.14	2.35	7.6 ± 0.3	6.5 ± 0.3	0.000 ± 0.002
0.008	0.57	2.34	8.2 ± 0.5	6.7 ± 0.4	0.000 ± 0.006
0.014	1.00	2.53	2.5 ± 0.4	2.1 ± 0.3	0.000 ± 0.002
0.040	2.86	2.50	2.3 ± 0.2	1.9 ± 0.2	0.002 ± 0.001
mixed		2.15	5.0 ± 0.3	4.1 ± 0.2	0.033 ± 0.013

the lowest χ^2 of the fits is found using populations with Z=0.001 (0.07 $Z_\odot$) suggest that this is a low stellar metallicity object. All spectral models obtained have low extinction (see Table 5) which is in good agreement with the previous results in Christensen et al. (2012a).

We obtain current stellar masses – the mass of the initial gas cloud assumed in burst models of stellar populations accounting for mass losses by winds and supernovae – of $M_\star = 6.7 \pm 0.2$, 6.5 ± 0.3, 6.7 ± 0.4, 2.1 ± 0.3, $1.9 \pm 0.2 \times 10^9$ $M_\odot$ for the lowest to the highest single-metallicity libraries and $M_\star = 4.1 \pm 0.2 \times 10^9$ $M_\odot$ for the mixed library. To derive this, we use the combined spectrum to ensure the highest signal-to-noise ratio possible, but rescale its continuum level to match the magnification-corrected flux of the central spectrum, which contains the total continuum flux. The

masses are marginally higher than the ones derived by Christensen et al. (2012a). The difference probably arises from the improved cluster mass model (and consequently the magnification factors) and a better estimate of the total flux with IFU data. Throughout the rest of the analysis, we assume that the mass of the galaxy is $6.7 \pm 0.2 \times 10^9$, the one obtained with the lowest metallicity library, the fit with the lowest $\chi 2$.

Another possible approach to the study of stellar populations is to analyse the He II λ1640 equivalent width that Brinchmann, Pettini & Charlot (2008) suggest as a metallicity and age indicator. As a very high ionization energy is needed to ionize He II, this line is an indicator of the presence of Wolf–Rayet stars, and can therefore be used as an age indicator. Because the equivalent width of He II will depend on the ratio of Wolf–Rayet and O stars which in turn depends on metallicity, it can also be used as a metallicity indicator. If we compare the measured equivalent width (∼1 Å) with the expected EW for continuous star formation models (see fig. 1 of Brinchmann et al. 2008) this value corresponds to stellar formation from about 3 Myr earlier. Although these are smoothed, simplified models of real star formation histories, this seems consistent with the younger stellar populations we found with the stellar population models fit (2–8 Myr). Nevertheless, an equivalent width of 1 Å implies a much higher stellar metallicity for these continuous star formation models: at least 0.4 $Z_\odot$ compared with the preferred 0.07 $Z_\odot$ from the stellar populations modelling. Brinchmann et al. (2008) also explore the effects of bursts, concluding that the equivalent width of He II could be strongly boosted for a very short period of time right after a recent episode of star formation which, in this case, would mean a boost of about 50 per cent in the strength of the He II line in order to achieve the lowest metallicities considered in their models (0.2 $Z_\odot$). Although we should be careful about drawing conclusions from the He II equivalent width, since the study was made for continuous star formation and simplified star formation histories, it seems to also point to the strong and recent burst scenario found with the full spectrum fitting.

4.2.4 *Stellar and ISM metallicity from absorption features*

From the previous stellar population analysis we find that it is not possible to constrain the stellar metallicity with confidence. This prompts us to explore another method, based on empirically calibrated equivalent widths of faint absorption UV features. Of the five possible metallicity indicators explored by Sommariva et al. (2012) – F1370, F1425, F1460, F1501, F1978 – we discard the first due to contamination by an intervening absorber and the last since sky residuals in this region are too high. To calculate the equivalent width of the remaining features, we normalize the spectrum following the procedure described in Rix et al. (2004): several continuum points, free of emission and absorption lines, are used to estimate the continuum level using a low-order spline. The equivalent width of the features within the spectral windows defined by Sommariva et al. (2012) is then estimated and the pseudo-continuum calibrations used to obtain the metallicity (see Fig. 9). The error is estimated by removing one of the continuum intervals at a time and recalculating the normalization and the equivalent width measurement, and the standard deviation of these measurements is taken as the error. The metallicities from the F1425 and F1460 indices agree to within an order of magnitude, but for the F1501 index the obtained metallicity is unphysical (Table 6). The obtained metallicities – $Z = 0.0424 \pm 0.0085$ $Z_\odot$ and 0.0678 ± 0.0078 $Z_\odot$ – are lower but still comparable with our best measurement from the stellar population analysis (0.07 $Z_\odot$), which is also the lowest possible metallicity in the STARBURST99 models, and which once more suggests that this is a low stellar metallicity system.

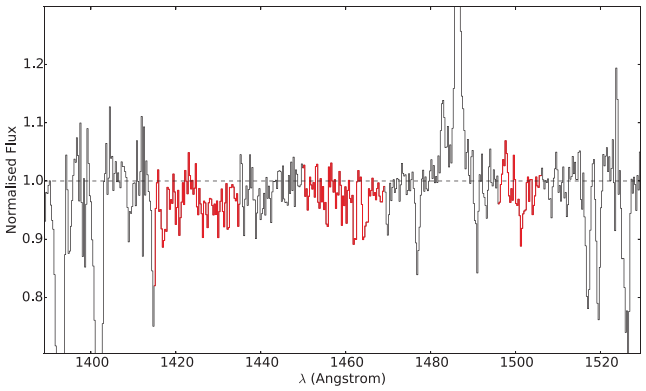

Figure 9. Equivalent widths of faint absorption features were estimated in three spectral windows (in red) of the normalized spectrum (in black). These were used as direct stellar metallicity estimators, following the work from Sommariva et al. (2012). Applying their calibrations, we derive a low stellar metallicity for the first two windows (F1425 and F1460 indices) of 0.0424 and 0.0678 $Z_\odot$, respectively.

Table 6. Direct metallicity estimations following the work of Sommariva et al. (2012).

Index	λ range	EW (Å)	$Z/Z_\odot$
F1425	1415–1435	0.3940 ± 0.0313	0.0424 ± 0.0085
F1460	1450–1470	0.4870 ± 0.0334	0.0678 ± 0.0078
F1501	1496–1506	-0.0271 ± 0.0316	INDEF

We also use a similar method to explore the ISM metallicity, following Leitherer et al. (2011) prescription to calculate the equivalent width of several ISM absorption lines. In their work, a sample of local galaxies with known metallicities is used to study how these features would correlate with metallicity, concluding that the Si II λ1260, O I and Si II λ1303 blend, C II λ1334 and Si II λ1526 absorptions are correlated to galaxy metallicity. In Fig. 10 we present the local galaxy measurements from fig. 15 of Leitherer et al. (2011), adding in our object for comparison. Although it is not possible to directly estimate metallicity following this method, our equivalent width measurements seem to follow the overall correlation of galaxies at low metallicities, with $12 + \log(\mathrm{O/H}) \sim 7.5$–$7.9$, which corresponds to a solar metallicity of 0.065 to 0.16 $Z_\odot$, a value that is comparable or slightly higher than the stellar metallicity, a trend that is found in other high-redshift galaxies (fig. 6 of Sommariva et al. 2012). Other gas metallicity indicators were reported in Christensen et al. (2012b): R23, Ne3O2 and a direct measurement, yielding metallicities of 7.74 ± 0.03, 7.56 ± 0.11 and 7.76 ± 0.03 in 12+log (O/H), respectively, compatible to our estimations from the comparison with the Leitherer et al. (2011) local galaxy sample.

We compare system 1 with the mass–metallicity relation derived at high redshift by using equation (2) of Mannucci, Salvaterra & Campisi (2011), we independently confirm the Christensen et al. (2012b) results placing this galaxy 0.6 dex (about 2 σ) below the mass–metallicity relation. Mass–metallicity outliers have been studied in the past in the local universe. In particular, Peeples, Pogge & Stanek (2009) investigated a set of massive galaxies, noticing that many had high SFRs and disturbed morphologies, indicating a

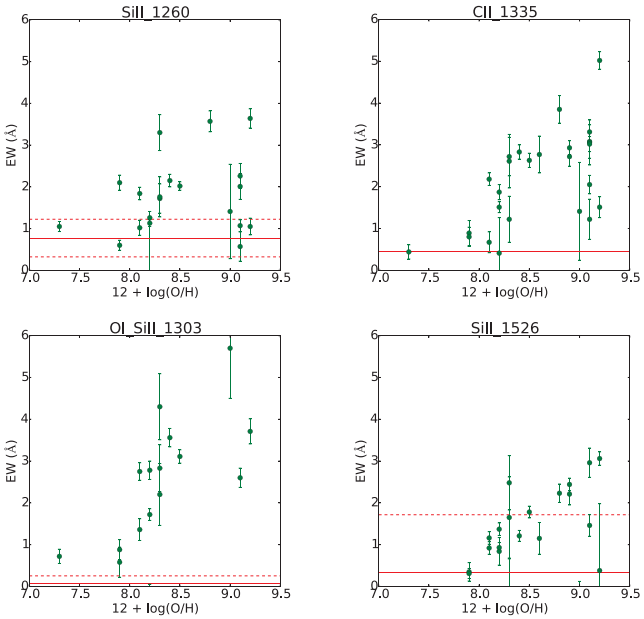

Figure 10. ISM metallicity trends of various indices from Leitherer et al. (2011). Green dots: data from local galaxies (fig. 15 of Leitherer et al. 2011). Red line: equivalent width obtained for system 1 (dashed lines correspond to the error). In order, the panels represent the Si II λ1260, O I and Si II λ1303 blend, C II λ1334 , Si II λ1526 features. All the above features point to a low-metallicity object, when compared with the local sample.

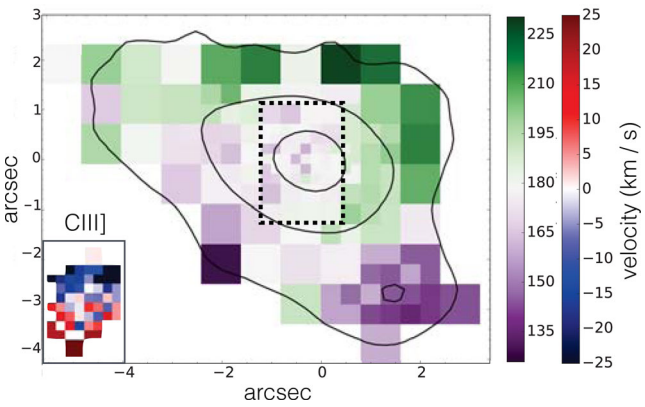

Figure 11. Lyα velocity map relative to systemic velocity. Small insert on left bottom corner: C III] velocity map, also relative to the systemic velocity, of the central part of the galaxy (marked with a black dotted rectangle in the Lyα image). It is worth noticing that the C III] velocity (which traces the gas kinematics) is not reproduced in the Lyα map, since not only kinematics but also resonant processes influence the frequency of the emitted photons.

possible merger. They argue that low-metallicity gas inflow induced by the merging could explain the offset in the metallicity–mass relation of those outliers. The close presence of the companion (see Section 3) and high SFR might suggest that an earlier interaction could be a valid scenario for this high-redshift galaxy, but we cannot exclude other possible explanations.

4.3 Resolved properties

In this subsection, we make use of the full power of MUSE and explore the spatial extent of Lyα emission as well as the spectral variations seen in both Lyα and other non-resonant lines across the galaxy. We focus this analysis on image 1.3, which covers the full extent of the source.

4.3.1 Emission line spatial variation

We define a small cube, centred on image 1.3, from which we extract the spectrum of each spaxel, fitting the Lyα line with an asymmetric Gaussian profile (see Section 4.1), and other nebular lines (C III] λλ1907, 09, O III] λλ1661, 66, N IV] λλ1483, 86) with a single Gaussian. All nebular lines are fitted simultaneously, using a single common redshift. We repeat this process following a quadtree method, spatially binning the small cube in 2 × 2 and 4 × 4 pixels, depending on the quality of the Lyα (or nebular lines) fit. This allows us to investigate fainter parts of the galaxy, although with a lower spatial resolution. The resulting maps can be seen in Fig. 11, with the peak shifts measured relative to the systemic redshift.

Apart from the companion, which is consistently blueshifted relative to the central part of the main body by approximately 30 km s^{-1}, there is no clear trend in the Lyα map. The C III] λλ1907, 09 map (inset in Fig. 11) shows variations on small spatial scales, with hints of a velocity gradient along the SE/NW direction, with an amplitude of ±25 km s^{-1}. In contrast, the central part of the Lyα map is very homogeneous with a mean redshift of 160–170 km s^{-1}. This is only in the external parts of the Lyα halo that the Lyα peak shows typical variations of at most ±40–50 km s^{-1}. Assuming that the bulk of the Lyα emission in this galaxy is produced from recombination in H II regions inside the ISM, we can interpret the velocity field shown by the C III] λλ1907, 09 map as the intrinsic velocity field of the Lyα emission, since C III] λλ1907, 09 is a nebular line produced in the same H II regions as Lyα. In other words, if Lyα were non-resonant, it would display the same velocity map as C III] λλ1907, 09. Undergoing multiple scatterings in the surrounding neutral gas, the Lyα radiation imprints the relative velocity of the scattering medium between its production site and its last scattering location: Lyα transfer in a static medium leads to a double-peaked profile; if the scattering medium is globally infalling on to the Lyα source, the emergent Lyα profile is blueshifted; and if the gas is outflowing, Lyα is redshifted (e.g. Neufeld 1990; Dijkstra 2014). The fact that the Lyα spectrum emerging from our halo is redshifted in every location is a probe that it scattered on to outflowing gas with respect to its production site. The asymmetric blue tail of the low ionization absorption lines confirms that there is outflowing gas in the ISM of this galaxy, at least in front of the stellar continuum, although the strongest absorption is not blueshifted, tracing also static gas. On top of the bulk velocity of the scattering medium, the width and the shift of the maximum of the Lyα peak correlate with the column density of the scattering medium (e.g. Verhamme et al. 2015). From the velocity map, the shift is between ∼150 and 200 km s^{-1} everywhere, which is typical of high-redshift LAEs (Hashimoto et al. 2015) tracing typical column densities of the order of log(NHI)∼20.

As previously stated, the companion Lyα peak shows a small but significant shift relative to the main body (∼30 km s^{-1}). Assuming that the two bodies are embedded in the same gas envelope, with the same column density and dust distribution, this difference would imply that the companion is in motion relatively to the main body. However, as stated above, since we do not have non-resonant lines that directly trace the kinematics of the companion, it is also possible to image a scenario where medium around the companion is less optically thick than around the main body, which would equally explain the observed shift.

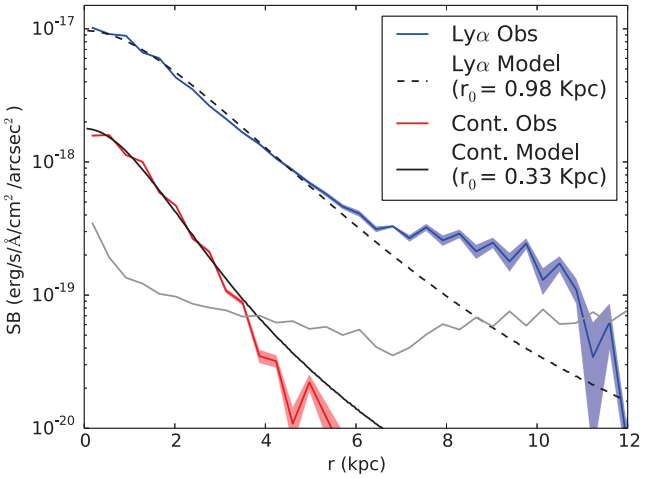

Figure 12. Blue: Lyα surface brightness profile measured in source plane, based on the source reconstruction of image 1.3. Red: same as previous, but from the continuum line image. Dashed line: exponential of scale length 0.98 kpc convolved with the MUSE PSF. Best match to the observed Lyα profile. Black line: same as before, but for the continuum profile. Grey line: 2 σ detection limit for Lyα alpha surface brightness.

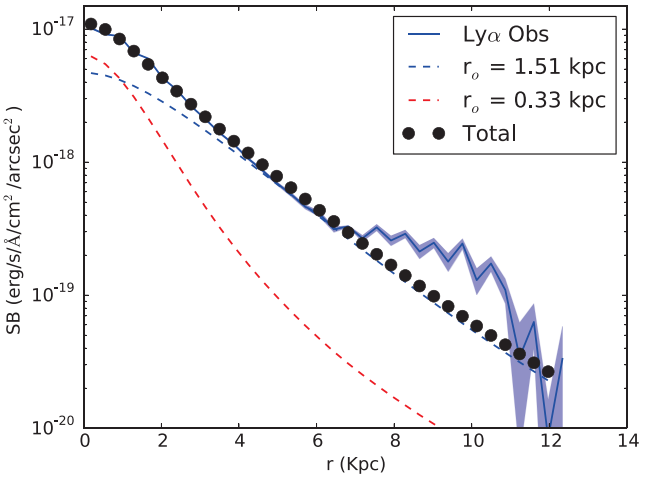

Figure 13. Blue: Lyα surface brightness profile measured in source plane, based on the source reconstruction of image 1.3. Dashed lines: two components of the two exponential model. Dots: combined two-exponential model compared with the previous (single-exponential) tested model; we are able to better reproduce the 6–7 kpc region. Nevertheless, the outer region (>10 kpc) is still not correctly reproduced.

4.3.2 Surface brightness profiles

To study the spatial extension of this object, we use the Lyα line image described in Section 2 as well as a continuum image, defined after inspecting the combined spectrum and selecting contiguous wavelength ranges free of emission or absorption lines, with a total width of 140 Åredward of Lyα. To prevent contamination from the nearby companion, we mask out the corresponding region(no. 3 in Fig. 4) in the images.

Both images are reconstructed in the source plane, where the galaxy shows an elliptical shape (mostly due to the PSF in the source plane). We measure the average surface brightness in elliptical annuli of 0.3 kpc width. The major/minor axis ratio of the ellipses is defined by the ratio of the FWHM of an elliptical 2D Gaussian fit to the Lyα line source plane image. The radius of the ellipse is converted into a circularized effective radius ($r = \sqrt{(b/a)} \times a$; Law et al. 2012) in kpc and the mean surface brightness is measured at each elliptical aperture in the Lyα and continuum images (see Fig. 12). Since these measurements are done in source plane, neighbouring pixels are highly correlated, so the noise level is estimated in the image plane and corrected for magnification and pixel rescaling. We also look for differences between profiles extracted along different radial orientations, once more excluding the companion, but find no significant deviations from the mean profile, indicating that the Lyα emission has a nearly isotropic shape.

In order to compare this result with other surface brightness studies it is important to disentangle the intrinsic size of the galaxy from what is observed due to the seeing. As a first approach, we assume that the intrinsic surface brightness profile can be well described with an exponential function: $s(r) = C\exp(-r/r_0)$, where s is the surface brightness at radius r and r_0 the scale length. To simulate the effects of the seeing, we build a sample of 2D exponential images with scale lengths varying from 0.2 to 2.0 kpc and convolve them with the source plane PSF. We then apply the same procedure used in the observations to obtain the surface brightness profile of these PSF convolved exponentials. Comparing the library of exponential radial profiles with the observations we find that the Lyα emission is best fitted by a scale length of 0.98 ± 0.03 kpc and the continuum by 0.33 ± 0.02 kpc. The continuum surface brightness intensity does not deviate significantly from an exponential profile (see Fig. 12), whereas the Lyα emission is higher than this simple model at $r >$ 4 kpc.

We compare this single exponential scale length with similar objects in the local Universe – the LARS (Hayes et al. 2013) – a sample of local (z <0.18) star bursting galaxies. Hayes et al. (2013) measure the Petrosian radius (R_{P20}) – the radius at which the local surface brightness is 20 per cent the average surface brightness inside of R – of 14 local galaxies finding that these are generally substantially larger in Lyα than in the FUV. As in the case of the scale lengths, it is desirable to compare intrinsic (deconvolved from the PSF) R_{P20} values, which we estimate by converting the intrinsic scale lengths with $R_{P20} = 3.62\, r_0$. We calculate a $R_{P20}^{Ly\alpha}$ of 3.5 kpc, a value that is a lower limit due to the mismatch between model and observations on the outskirts of the galaxy, and 1.2 kpc for the continuum Petrosian radius. Comparing this with fig. 3 from Hayes et al. 2013, we confirm that this galaxy is comparable to this sample of local galaxies regarding Lyα/continuum extension in both absolute and relative scales of Lyα and continuum.

We cannot directly compare these values with the ones obtained from stacking of LBGs and LAEs (e.g. Steidel et al. 2011) because in these studies only the more extended part of the profile are fitted, discarding the central region. Additionally, our previous approach does not fully reproduce the Lyα profile in the outer part of the galaxy, which prompts us to try to disentangle the contribution of the central part of the galaxy from the halo. To do this, we follow the approach introduced by Wisotzki et al. (2015) and model the emission as the sum of two exponentials, one aiming to reproduce the central emission originating from the star-forming regions and the other the more extended gaseous halo. We once more make a library of PSF convolved profiles, and fix the scale length of the inner part to the one obtained from the continuum emission fit (0.33 kpc), obtaining a Lyα 'halo' scale length of 1.51 ± 0.18 kpc (Fig. 13). This new model brings some improvements compared to the simple exponential: the $4 < r < 7$ kpc zone is now accurately reproduced. There is still a mismatch at larger radii, where the observations show

an even more extended emission, which would require a scale length of ∼5 kpc, as estimated from the slope measured in the 8–12 kpc region.

Comparing the scale lengths of 0.33 and 1.51 kpc (continuum and Lyα, respectively) with typical values obtained in high-redshift studies is not easy, since system 1 is less massive and smaller system than the high-redshift sources usually studied. For example, the continuum scale length of this particular object is 10 times smaller than typical lengths of the Steidel et al. (2011) sample. In a similar study, Momose et al. (2014) also make a careful analysis of stacked images in redshift bins from 2 to 6.6, finding a Lyα scale length of 5 to 10 kpc, for a redshift close to 3.5, which is higher than the scale length we obtained from the double exponential fit. This is nevertheless comparable to what we directly measure on the 8–12 kpc region, although we cannot confidently argue that this region in this particular object corresponds to the extended emission measured in Momose et al. (2014). We choose to instead compare the r_0(Lyα)/r_0(Continuum) ratio, to test if the extent of Lyα relative to the continuum in our small object is comparable to that of bigger objects: i.e. does the Lyα extension depend on the nature/mass/environment of galaxies? Using the Lyα scale length from the double exponential model, we obtain a ratio of 4.6, whereas Steidel et al. (2011) obtain a ratio of 7.4 for the global sample of LBGs and 8.8 for a subsample of Lyα emitters, suggesting that this system Lyα emission is less extended than these bigger objects compared to the continuum emission. We note that some of the differences may arise from the surrounding Mpc-scale environment, particularly the density of the circum-galactic medium, as concluded by Matsuda et al. (2012). Wisotzki et al. 2015 recently used the newly obtained MUSE data set on the Hubble Deep Field South (Bacon et al. 2015) to study a relatively large (26) sample of Lyα emitters on an object-to-object basis. These are galaxies with comparable or slightly larger scale lengths both in Lyα and in continuum emission. Directly comparing the scale lengths we find two other sources in the HDFS sample at $z = 4$ with very similar values, although the Lyα/continuum ratio in our galaxy is slightly smaller than the typical ratio (∼5–10) of the Wisotzki et al. (2015) sample.

It is worth noticing that our error bars only include statistical errors. Systematics errors can affect the relative weights of the data points in the central part and the outskirts and be the source of the mismatch seen at $r > 7$ kpc. To test this we increased the relative errors in the central region to a constant value of 5 per cent, matching the errors at 6 kpc where the observations start to deviate from the fit. Under this weighting scheme we would obtain a larger scale length ($r_o = 2.7$ kpc) for Lyα in the double-exponential model, but the fit still does not reproduce the observations at $r > 7$ kpc. We alternatively tested the use of Sérsic profiles with $1 < n < 10$ for the extended halo component but they did not provide a better fit in this region.

5 LYMAN α MODELLING

In this section we model the Lyα emission using a radiative transfer code predicting the spectra emerging from spherically expanding shells (Verhamme, Schaerer & Maselli 2006). In our first approach, we fit the Lyα line using the usual library produced by the radiative transfer code, deriving the physical parameters that better describe the total and companion spectra. In the second part we try, for the first time, to test if the same simple expanding shell model can simultaneously describe the three main body spectra (central, halo, total).

5.1 Fitting of individual spectra with expanding shells

We separately fit the spectra of the main body and the companion with our library of synthetic spectra (Schaerer et al. 2011) which are characterized by four physical parameters:

(i) the radial expansion velocity $v_{\rm exp}$,
(ii) the radial column density $N_{\rm H\,I}$,
(iii) the Doppler parameter b encoding thermal and turbulent motions,
(iv) the dust absorption optical depth $\tau_{\rm d}$, linked to the extinction by $E(B-V) \sim (0.06...0.11)\,\tau_{\rm d}$,

the lower numerical value corresponding to a Calzetti attenuation law for starbursts, and the higher to the Galactic extinction law from Seaton (1979). The intrinsic Lyα emission, before transfer, is modelled as a Gaussian plus continuum with two parameters: the intrinsic EW(Lyα) and the intrinsic FWHM(Lyα) of the profile. This library has already been successfully used to model Lyα profiles from high-redshift star-forming galaxies (Verhamme et al. 2008; Dessauges-Zavadsky et al. 2010; Vanzella et al. 2010; Lidman et al. 2012; Hashimoto et al. 2015), but also in the local Universe (Atek, Schaerer & Kunth 2009; Leitherer et al. 2013, Orlitova et al., in preparation).

In order to limit the number of free parameters, we redshift the synthetic spectra to the observed redshift $z = 3.50618$; we fix the FWHM of the intrinsic Lyα profile to 140 km s^{-1}, the mean FWHM of the nebular lines as measured in the observed total spectrum, and we allow for only low extinction values, $0 < E(B-V) < 0.05$, consistent with our stellar population results (Section 4.2.3). The results are presented in Fig. 14, and the best-fitting parameters are summarized in Table 7.

Reasonable fits are obtained for both spectra, although the extension of the red wing is not well reproduced. The best-fitting values of the parameters are very similar for both spectra, which may be expected given their similar shapes. The obtained expansion velocity is 100 km s^{-1} for both spectra and the column density is in the range $19 < \log(N_{\rm H\,I}) < 20$ for the 10 best fits of each object, corresponding to typical values obtained in similar studies of high-redshift Lyα emitters. Compared with the results obtained by Christensen et al. (2012b), who used a combination of hydrogen clouds and an expanding shell, we derive similar parameters for the column density and shell properties (Table 7), but higher intrinsic equivalent width. This difference probably comes from the lower reddening in their model.

We should keep in mind that our model is an oversimplification of the circumgalactic gas around our object, which has certainly a more complex density and velocity distributions than the assumed homogeneous shell expanding at a single velocity. From the absorption profiles of the low ionization lines (see Fig. 6) we see a distribution of velocities and densities, with most of the gas being static or slowly expanding, but also outflowing material up to 500 km s^{-1}. The velocity and the column density values derived from the Lyα fitting can be interpreted as the effective velocity and column density seen by Lyα in this object and although they provide us with (at least) the right order of magnitude,[1] they are not direct

[1] Blind fitting of noisy synthetic spectra from expanding shells has been recently studied in detail by Gronke, Bull & Dijkstra (2015), demonstrating that degeneracies exist among some parameters of the 'expanding shell' model, but the column density and the expansion velocity are always accurately recovered.

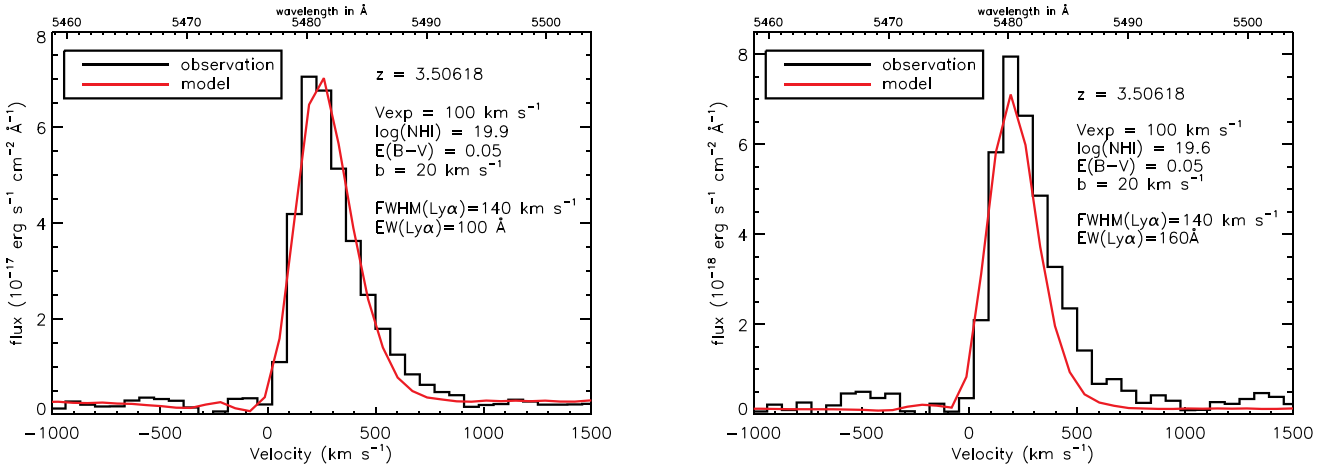

Figure 14. Best fits of synthetic Lyα spectra from homogeneous expanding shells to two different extracted MUSE spectra. Left: total Lyα spectrum of System 1.3 in SMACS2031. Right: Lyα spectrum extracted from the companion. The models perform well on the bluer side of the peak emission, also correctly reproducing the peak, but fail to completely reproduce the red wing, predicting less flux than the one observed. Both models have similar physical parameters.

Table 7. Best-fitting values obtained by comparing the observed spectra to synthetic spectra emergent from a homogeneous expanding shell model containing six parameters: two that define the intrinsic Lyα emission (EW$_{\rm int}$(Lyα) and FWHM$_{\rm int}$(Lyα) in km s^{-1}) and four others that describe the physical parameters of the shell (see text for a detailed description).

Region	z	EW$_{\rm int}$(Lyα)	FWHM$_{\rm int}$(Lyα)	$v_{\rm exp}$ (km s^{-1})	log ($N_{\rm H\,I}$) (cm^{-2})	b (km s^{-1})	$E(B-V)$	$\chi^2_{\rm ref}$
Christensen+12	3.5073	20	N/A	110	20.7*	10	0.01	N/A
Total	3.506 18	100	140	100	19.9	20	0.05	304
Companion	3.506 18	144	140	100	19.6	20	0.05	14
Central	3.506 18	100	140	100	19.9	20	0.05	245
Halo	3.506 18	100	140	100	19.9	20	0.05	244

*Equivalent column density from clouds model.

measures and the real gas distribution is more complex than what can be learned from these models.

5.2 Comparison of synthetic spectra and surface brightness with observations

We now propose to further test the expanding shell model, by computing the synthetic surface brightness profile and peak shift map as well as spectra from the central and halo regions from our best-fitting model, and directly comparing them with the available observables. The library of models used so far is not suitable to do this exercise since the spatial information (last scattering location of each photon before escape) is not computed and stored. For this reason we had to rerun the Lyα radiation transfer simulation corresponding to the best-fitting model of the global spectrum to retrieve this information.

From this new simulation, we build a synthetic data cube: for each photon, we compute the radius of the last scattering location on to the projected image of the shell perpendicular to the escape direction. Thanks to the spherical geometry of our problem, the contribution of all photons is stacked to obtain a distribution of projected radii. Knowing the frequency and luminosity of each photon with a given r, we sample this distribution on to a 3D cube with two spatial dimensions and a spectral dimension. Our synthetic cube has 101 × 101 × 101 pixels, with a spectral range from ∼1205 to 1232 Å in rest frame, but no physical spatial scale, except for the fact that the ionizing radiation is emitted from a central point source, infinitely small compared to the radius of the expanding shell. The last step before building meaningful observables is the convolution of the cube with the MUSE PSF and LSF. For the PSF, it is necessary to assume a model physical scale, since it has a fixed size (that we convert to kpc in the source plane). The synthetic surface brightness profile will change depending on the assumed scale, and we use this fact to calculate a physical scale by fitting the observed Lyα surface brightness with the surface brightness extracted from a synthetic Lyα image (5480 to 5490 Å) following exactly the same methodology used in the data (see Section 4.3.2). After completing these steps, we are left with a synthetic data cube spatially and spectrally comparable with the observations.

The next step is to define central and halo regions in the model equivalent to the ones defined in the observations. We use the observed Lyα flux ratio obtained from the observed data – the central region contains approximately 40 per cent of the total flux and the halo 60 per cent (see Section 3) – and integrate the escaping photons from the model in elliptical annuli of increasing size (to compensate for the asymmetry of the PSF) until the fluxes from the model 'central' and 'halo' regions match the observed fluxes. We fit the total observed spectrum with the total synthetic spectrum, obtaining a flux normalization factor that we use to rescale the synthetic central and halo spectra to their expected flux and compare them with the observations (see Fig. 15). Both synthetic surface brightness profiles of continuum and Lyα are in good agreement with the observations, although the synthetic surface brightness profile is flatter than the observations at large radii. Interestingly, the synthetic central and halo spectra fit quality is very similar to the one of the total spectrum: the global shape is well reproduced, but they cannot fit the extension of the red wing. We assumed a radius for the gas shell of 54 kpc, which corresponds to a total hydrogen mass

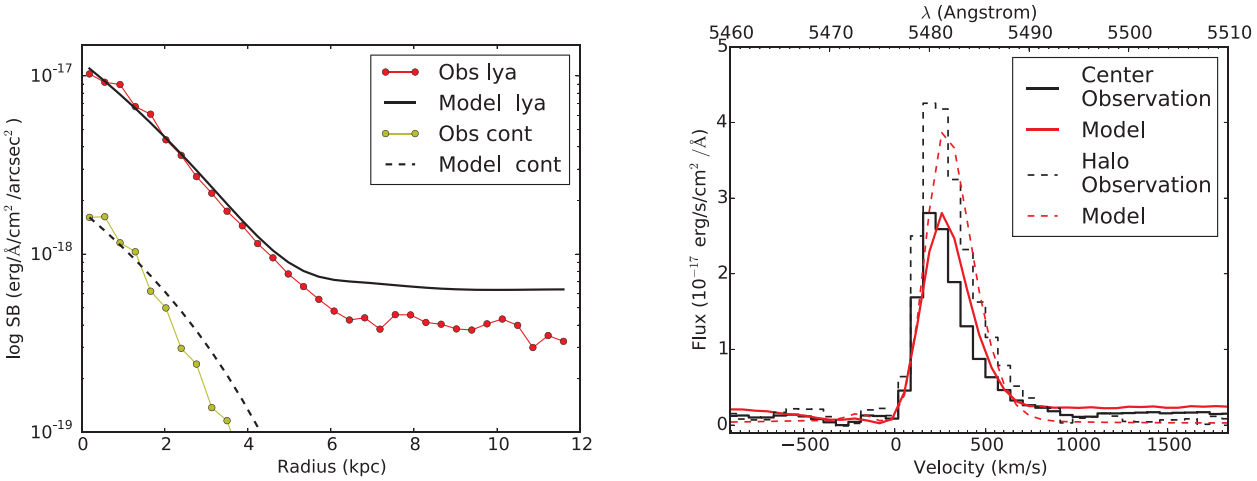

Figure 15. Left: surface brightness profiles from observations (dotted lines) and radiative transfer models in an expanding gas shell (black lines) after PSF convolution. A good agreement between model and observations is obtained in the inner region for Lyα and C III] $\lambda\lambda$1907, 09. However at larger radii the model predicts more Lyα flux than observed. Right: observed and best model central spectrum in full lines (black and red, respectively) and observed halo and best model halo spectra, in dashed. The small velocity difference between central and halo region is correctly predicted by the model and it is interesting to notice that these fits reproduce the observations with the same quality as the one obtained with the global spectrum.

in the shell of $\sim 2 \times 10^9$ M$_\odot$, about a third of what we obtained for the stellar mass.

Given the spherical symmetry of our geometry, the velocity maps show a radial gradient with the peak of the Lyα profile slightly shifting further away from line centre with radius, with an increase of the order of $\sim$50 km s^{-1} for our best fit. This variation between central and edge is compatible with what we observe in the upper-right edge of the velocity map. The main difference between the observed Lyα maps and the model is the asymmetry seen in the observations, where the concentric distribution of velocities is not seen. This is not completely unexpected, due to the simplicity of the expanding shell model, which assumes, for example, a single shell of uniform density, a single ionizing Lyα source, while *HST* data show at least two star-forming regions in this galaxy, and does not account for possible interactions with nearby objects (does the companion interact with the gas?).

Overall, we conclude that the strong and diverse constraints provided by this observation are generally reproduced by a simple expanding shell model, which can altogether fit the integrated spectrum, the spatially resolved spectra, the surface brightness profile and the shift of the line peak with radius with good accuracy, although not perfectly. Alternative, more complex models have been suggested, for example incorporating biconical outflows (Mas-Hesse et al. 2003; Swinbank et al. 2007; Dijkstra & Kramer 2012; Laursen, Duval & Östlin 2013), which are beyond the scope of this study.

Finally, we combine information derived from the integrated spectrum and the expanding shell model to study the energetics of the gas outflow. We do so mainly following the considerations of Swinbank et al. (2007), but estimating the shell parameters (mass and size) from the Lyα radiative transfer model. From the stellar population analysis, a recent ($\sim$10 Myr) period of star formation is seen. Assuming that this episode was responsible for the expansion of the shell, that the UV SFR (17.5 M$\odot$ yr^{-1}) does not change within this period and that SNe provide 10^{49} ergs per M$_\odot$ (e.g. Benson et al. 2003), we estimate that there are $\sim 2 \times 10^{57}$ erg available from star formation. Assuming an expanding velocity of 100 km s^{-1} and the shell mass derived in the previous section ($\sim 2 \times 10^9$ M$_\odot$) we obtain a kinetic energy of $\sim 2 \times 10^{56}$ erg. We also estimate the gravitational influence of a dark matter halo of $10^{11.8}$ M$_\odot$ (typical for such a galaxy at these redshift, e.g. Moster, Naab & White 2013) in the shell expansion. If we assume a simple point source scenario to calculate the loss of potential energy up to a 54 kpc radius, we obtain a loss of potential energy of $\sim 5 \times 10^{56}$ erg. Bearing in mind that these are rough estimations, we obtain a coupling factor between the radiative energy from star formation and the gas of $\sim$35 per cent.

6 SUMMARY

We present new observations of a high-redshift ($z = 3.5$) L* galaxy, obtaining exceptional spectra quality thanks to both the magnification of gravitational lensing and the high-sensitivity spatial coverage and resolution of MUSE. We summarize our main results below:

(i) The high signal-to-noise rest-frame UV spectrum contains a wealth of emission and absorption lines, which we combine to derive physical properties (density, temperature, gas covering fraction), in the central kpc of this young $\sim 6 \times 10^9$ M$_\odot$ galaxy.

(ii) We spatially resolve the extended Lyα emission and its velocity, as well as, for the first time, the associated C III] kinematics in the central region. The Lyα emission has a very uniform profile across $\sim$10 kpc, showing only a small velocity shift that is unrelated to the intrinsic kinematics of the nebular emission.

(iii) We identify a companion object, previously unknown, located 11.2 kpc away, only detected in Lyα emission. The line profile is similar profile to the main object, although blueshifted by 20 km s^{-1}.

(iv) We find that both stellar population fitting and direct estimations yield compatible stellar metallicities: 0.07 and 0.05 Z$_\odot$. We derive an ISM metallicity of 0.016–0.065 Z$_\odot$, which agrees with previously derived ISM metallicities and also confirms that this particular object is $\sim 2\,\sigma$ lower than the expected mass–metallicity relation.

(v) The Lyα emission is more extended than the continuum emission, with length scales of 1.51 kpc and 0.34 kpc, respectively.

Comparing this with the results of stacked images, this galaxy seems more compact (Lyα is less extended relatively to continuum) than what is obtained for bigger and more massive galaxies at equivalent redshifts. Nevertheless, this object is comparable with the local LARS and to some individual galaxies from the HUDF LAE sample.

(vi) The observed Lyα line is well fitted by synthetic spectra generated from a spherically expanding $\sim 2 \times 10^9$ $M_\odot$ gas shell model. We further test this model by comparing the predicted surface brightness and predicted central and halo spectra and conclude that this simple model is compatible with the observations.

In our Lyα analysis, we not only fit the Lyα spectral-profile, but also compare the predicted resolved properties, such as spatially resolved spectra, velocity maps and surface brightness profile with observations. The discrepancies seen between the simulated and observed Lyα properties, despite their general qualitative agreement, demonstrate that the quality of the presented observations represents a challenge to current models, and show the power of such a comparison and the need for further studies of resolved LAEs to improve our understanding of Lyα properties. Future observations of lensing clusters, as part of the MUSE guaranteed time observations, will allow us to find more examples of such sources at high redshift, which might constitute a rich testing sample not only for Lyα radiative transfer codes predictions, but also for other galaxy evolution features, such as structure formation and chemical enrichment.

ACKNOWLEDGEMENTS

We thank the referee for providing useful comments on the submitted version that improved the clarity and content of this work as well as Claudia Scarlata, Dan Stark and Thibault Garel for insightful and stimulating discussions. VP, JR, DL and BC acknowledge support from the ERC starting grant CALENDS. JR acknowledges support from the CIG grant 294074. AV is supported by a Fellowship Boursière d'Excellence of Geneva University. RB acknowledges support from the ERC advanced grant 339659-MUSICOS. JR, TC and GS acknowledge support of the ANR FOGHAR (ANR-13-BS05-0010-02). LC is supported by YDUN/DFF k 4090-00079.

REFERENCES

Atek H., Schaerer D., Kunth D., 2009, A&A, 502, 791
Bacon R. et al., 2010, in SPIE Conf. Ser. Vol. 7735. The MUSE Second-generation VLT Instrument. p. 8
Bacon R. et al., 2015, A&A, 575, A75
Bayliss M. B., Rigby J. R., Sharon K., Wuyts E., Florian M., Gladders M. D., Johnson T., Oguri M., 2014, ApJ, 790, 144
Behrens C., Dijkstra M., Niemeyer J. C., 2014, A&A, 563, A77
Benson A. J., Bower R. G., Frenk C. S., Lacey C. G., Baugh C. M., Cole S., 2003, ApJ, 599, 38
Bian F. et al., 2010, ApJ, 725, 1877
Bouché N., Hohensee W., Vargas R., Kacprzak G. G., Martin C. L., Cooke J., Churchill C. W., 2012, MNRAS, 426, 801
Brinchmann J., Pettini M., Charlot S., 2008, MNRAS, 385, 769
Cabanac R. A., Valls-Gabaud D., Lidman C., 2008, MNRAS, 386, 2065
Calzetti D., Armus L., Bohlin R. C., Kinney A. L., Koornneef J., Storchi-Bergmann T., 2000, ApJ, 533, 682
Christensen L. et al., 2012a, MNRAS, 427, 1973
Christensen L. et al., 2012b, MNRAS, 427, 1953
Cid Fernandes R., Mateus A., Sodré L., Stasińska G., Gomes J. M., 2005, MNRAS, 358, 363
Dessauges-Zavadsky M., D'Odorico S., Schaerer D., Modigliani A., Tapken C., Vernet J., 2010, A&A, 510, A26
Dijkstra M., 2014, 31, 40
Dijkstra M., Kramer R., 2012, MNRAS, 424, 1672
Ebeling H., Edge A. C., Henry J. P., 2001, ApJ, 553, 668
Erb D. K., Pettini M., Shapley A. E., Steidel C. C., Law D. R., Reddy N. A., 2010, ApJ, 719, 1168
Erb D. K. et al., 2014, ApJ, 795, 33
Fosbury R. A. E. et al., 2003, ApJ, 596, 797
Garel T., Guiderdoni B., Blaizot J., 2015, MNRAS, 455, 3436
Gronke M., Bull P., Dijkstra M., 2015, ApJ, 812, 123
Hainline K. N., Shapley A. E., Kornei K. A., Pettini M., Buckley-Geer E., Allam S. S., Tucker D. L., 2009, ApJ, 701, 52
Hashimoto T. et al., 2015, ApJ, 812, 157
Hayes M. et al., 2013, ApJ, 765, L27
Hayes M. et al., 2014, ApJ, 782, 6
Henry A., Scarlata C., Martin C. L., Erb D., 2015, ApJ, 809, 19
James B. L. et al., 2014, MNRAS, 440, 1794
Jones T., Ellis R. S., Richard J., Jullo E., 2013a, ApJ, 765, 48
Jones T. A., Ellis R. S., Schenker M. A., Stark D. P., 2013b, ApJ, 779, 52
Kennicutt R. C., Jr, 1998, ApJ, 498, 541
Kroupa P., 2001, MNRAS, 322, 231
Laursen P., Duval F., Östlin G., 2013, ApJ, 766, 124
Law D. R., Steidel C. C., Shapley A. E., Nagy S. R., Reddy N. A., Erb D. K., 2012, ApJ, 759, 29
Leitherer C. et al., 1999, ApJS, 123, 3
Leitherer C., Tremonti C. A., Heckman T. M., Calzetti D., 2011, AJ, 141, 37
Leitherer C., Chandar R., Tremonti C. A., Wofford A., Schaerer D., 2013, ApJ, 772, 120
Lidman C., Hayes M., Jones D. H., Schaerer D., Westra E., Tapken C., Meisenheimer K., Verhamme A., 2012, MNRAS, 420, 1946
Luridiana V., Morisset C., Shaw R. A., 2012, A&A, 573, A42
Mannucci F., Salvaterra R., Campisi M. A., 2011, MNRAS, 414, 1263
Mas-Hesse J. M., Kunth D., Tenorio-Tagle G., Leitherer C., Terlevich R. J., Terlevich E., 2003, ApJ, 598, 858
Matsuda Y. et al., 2012, MNRAS, 425, 878
Momose R. et al., 2014, MNRAS, 442, 110
Morales-Luis A. B., Pérez-Montero E., Sánchez Almeida J., Muñoz-Tuñón C., 2014, ApJ, 797, 81
Moster B. P., Naab T., White S. D. M., 2013, MNRAS, 428, 3121
Neufeld D. A., 1990, ApJ, 350, 216
Peeples M. S., Pogge R. W., Stanek K. Z., 2009, ApJ, 695, 259
Pettini M., Rix S. A., Steidel C. C., Hunt M. P., Shapley A. E., Adelberger K. L., 2002, Ap&SS, 281, 461
Prescott M. K. M., Momcheva I., Brammer G. B., Fynbo J. P. U., Møller P., 2015, ApJ, 802, 32
Quider A. M., Pettini M., Shapley A. E., Steidel C. C., 2009, MNRAS, 398, 1263
Richard J. et al., 2015, MNRAS, 446, L16
Rivera-Thorsen T. E., Hayes M., Östlin G., Duval F., Orlitová I., Verhamme A., Mas-Hesse J. M., Schaerer D., 2015, ApJ, 805, 14
Rix S. A., Pettini M., Leitherer C., Bresolin F., Kudritzki R.-P., Steidel C. C., 2004, ApJ, 615, 98
Schaerer D., Hayes M., Verhamme A., Teyssier R., 2011, A&A, 531, A12
Seaton M. J., 1979, MNRAS, 187, 73p
Shapley A. E., Steidel C. C., Pettini M., Adelberger K. L., 2003, ApJ, 588, 65
Sommariva V., Mannucci F., Cresci G., Maiolino R., Marconi A., Nagao T., Baroni A., Grazian A., 2012, A&A, 539, A136
Stark D. P., Swinbank A. M., Ellis R. S., Dye S., Smail I. R., Richard J., 2008, Nature, 455, 775
Stark D. P., Schenker M. A., Ellis R., Robertson B., McLure R., Dunlop J., 2013, ApJ, 763, 129
Steidel C. C., Erb D. K., Shapley A. E., Pettini M., Reddy N., Bogosavljević M., Rudie G. C., Rakic O., 2010, ApJ, 717, 289
Steidel C. C., Bogosavljević M., Shapley A. E., Kollmeier J. A., Reddy N. A., Erb D. K., Pettini M., 2011, ApJ, 736, 160
Swinbank A. M., Bower R. G., Smith G. P., Wilman R. J., Smail I., Ellis R. S., Morris S. L., Kneib J.-P., 2007, MNRAS, 376, 479
Swinbank A. M. et al., 2009, MNRAS, 400, 1121

Swinbank M. et al., 2015, MNRAS, 449, 1298
Vanzella E. et al., 2009, ApJ, 695, 1163
Vanzella E. et al., 2010, ApJ, 725, 1011
Verhamme A., Schaerer D., Maselli A., 2006, A&A, 460, 397
Verhamme A., Schaerer D., Atek H., Tapken C., 2008, A&A, 491, 89
Verhamme A., Orlitová I., Schaerer D., Hayes M., 2015, A&A, 578, A7
Villar-Martín M., Cerviño M., González Delgado R. M., 2004, MNRAS, 355, 1132
Weijmans A.-M., Bower R. G., Geach J. E., Swinbank A. M., Wilman R. J., de Zeeuw P. T., Morris S. L., 2010, MNRAS, 402, 2245
Weilbacher P. M., Streicher O., Urrutia T., Pécontal-Rousset A., Jarno A., Bacon R., 2014, in Manset N., Forshay P., eds, Proc. ASP Conf. Ser., Vol. 485, Astronomical Data Analysis Software and Systems XXIII. Astron. Soc. Pac., San Francisco, p. 451
Wisotzki L., Bacon R., Blaizot J., Brinchmann J., Herenz E. C., Schaye 2015, A&A, preprint (astro-ph/1509.05143)
Wuyts E., Rigby J. R., Sharon K., Gladders M. D., 2012, ApJ, 755, 73
Yuan T.-T., Kewley L. J., Swinbank A. M., Richard J., Livermore R. C., 2011, ApJ, 732, L14

APPENDIX A:

We describe here the information that can be retrieved from the intervening absorbers detected in the spectrum of System 1. By reconstructing the source plane image at each redshift we were able to derive the impact parameters for the three systems, 33 kpc for s2, 41 kpc for system 12 and 26 kpc for system 4 (proper coordinates). From the same MUSE data set, the spectrum of the intervening systems galaxies was also extracted and examined [see fig. 3 from Richard et al. (2015) for systems 4 and 12]. System 4 has a very faint continuum, and only the Lyα line can be identified, so not much information could be derived. As for system 12 and s2, both had enough signal in the continuum to allow us to measure systemic redshift from other lines than Lyα (C IV doublet in absorption for both systems) as well as to derive stellar mass and SFR (Table A2) using the same procedure as described in Section 4.2.3.

One of the questions that can be addressed by the study of intervening absorbers is whether we are probing in-falling gas or an outflow (or galactic wind) and what are their characteristics. It has been proposed that the azimuthal angle (the angle between the disc of the absorbing galaxy and the direction of the illuminating system) can be used to make the distinction between an outflow or an inflow through geometrical arguments: moving gas close to the disc vertical direction (azimuthal angles close to 90°) has its most probable origin in galactic winds, since this is the only mechanism that can produce cool material systematically along the minor axis (Bouché et al. 2012). Comparing our azimuthal angles with the bimodal distribution obtained in Bouché et al. (2012), we see that s2 is consistent with being in the inflow group but that system 12 is still compatible with the galactic wind hypothesis. This last system gas has a Δv of 144 km s^{-1} and a specific SFR of 9.94 Gyr^{-1}. We briefly compare our results to those from Steidel et al. (2010), who used stacks of low-resolution spectra from star-forming galaxies at $z\sim2.5$ to obtain the typical equivalent widths of intervening absorption lines as a function of impact parameter. While we find that our rest-frame Si IV equivalent width (0.45±0.02Å) agrees well with theirs (0.39±0.08 Å at a mean impact parameter of 31 proper kpc), system 12 shows a significantly lower equivalent width of C IV. Specifically, since Steidel et al. (2010) do not resolve the C IV doublet, to facilitate comparison we add our two components together to obtain a rest-frame C IV EW of 0.498±0.001 Å (while Steidel et al. 2010 obtain 2.13±0.15 Å). This discrepancy could be attributed to, i.e. differences in ionization state or relative abundances, however, we leave a more detailed analysis to a future work.

Table A1. Absorption lines not identified as system 1 lines. Given wavelengths are in observed frame and in air and equivalent widths in observed frame. Last columns match the observed line with one of the intervening systems taken from Richard et al. (2015), when the identification was possible, otherwise a label is given.

λ_{obs} (Å)	EW (Å)	Line (Å)	z	System
5550.68	1.15 ± 0.074	Si IV	2.984	s2
5737.58	0.40 ± 0.198	(1)		
5766.45	0.63 ± 0.034	(2)		
5775.84	2.15 ± 0.127	Hγ	0.331	Cluster
6081.24	0.46 ± 0.021	Si II	2.984	s2
6153.12	1.99 ± 0.074	Si IV	3.414	System 12
6166.40	2.71 ± 0.027	C IV	2.984	s2
6176.66	2.04 ± 0.012	C II	2.984	s2
6192.28	1.44 ± 0.076	Si IV	3.414	System 12
6374.71	0.92 ± 0.056	(3)		
6622.59	0.22 ± 0.090	Si II	1.158	s4
6654.27	0.51 ± 0.052	Al II	2.984	s2
6718.53	0.30 ± 0.090	C IV	3.340	System 4
6729.72	0.03 ± 0.090	C IV	3.340	System 4
6835.88	1.10 ± 0.002	C IV	3.414	System 12
6847.26	1.10 ± 0.004	C IV	3.414	System 12
9127.71	2.84 ± 0.383	Mg II	2.2653	(*)
9152.61	2.75 ± 0.383	Mg II	2.2653	(*)

(*) Absorber probably related to system 11 ($z = 2.256$).

Table A2. Physical parameters derived for the s2 and system 12 absorbers, respectively. z_{sys} was measured in absorption lines (and emission lines whenever possible) on the absorber spectrum and z_{int} from the absorption lines seen in the spectrum of system 1. Mass and SFR were estimated with the same techniques as for system 1 (see Section 4.2.3). Inclination (θ), azimuthal angle (α), and impact parameter (b) were measured on the reconstructed source plane images of each system.

Parameter	Unit	s2	sys12
z_{sys}		2.9840	3.4162
z_{int}		2.9850	3.4141
Δv	[km s^{-1}]	−79 ±40	144 ± 32
Mass	[log ($M_\star$/M$_\odot$)]	8.40	9.29
SFR	[M$_\odot$ yr^{-1}]	2.1	5.1
θ	[deg]	46	27
α	[deg]	25.5	64
b	[kpc]	33	41

This paper has been typeset from a TEX/LATEX file prepared by the author.